Research Square

Preprints are preliminary reports that have not undergone peer review.
They should not be considered conclusive, used to inform clinical practice,
or referenced by the media as validated information.

Probabilistic Hazard Assessment of Pyroclastic Density Currents at Atitlán Stratovolcano, Guatemala

Eduard Pico Rodríguez

eduardpicor@geociencias.unam.mx

Universidad Nacional Autónoma de México

Lucia Capra Pedol

Universidad Nacional Autónoma de México

Sylvain Charbonnier

University of South Florida

Rafael Torres-Orozco

Universidad Nacional Autónoma de México

Rudiger Escobar-Wolf

Michigan Technological University

Omar Cruz-Vázquez

Universidad Nacional Autónoma de México

Research Article

Keywords: Pyroclastic density currents, Probabilistic hazard assessment, Titan2D, VolcFlow, Monte Carlo simulation, Atitlán volcano, Guatemala

Posted Date: November 13th, 2026

DOI: https://doi.org/10.21203/rs.3.rs-10748944/v1

License: This work is licensed under a Creative Commons Attribution 4.0 International License.
Read Full License

Additional Declarations: No competing interests reported.

Probabilistic Hazard Assessment of Pyroclastic Density Currents at Atitlán Stratovolcano, Guatemala

Eduard Pico Rodriguez[1, *], Lucia Capra Pedol[1, a], Sylvain Charbonnier[2,b], Rafael Torres–Orozco[1, c], Rudiger Escobar Wolf[3,d], Omar Cruz–Vázquez [1, e]

[1] Instituto de Geociencias, Campus Juriquilla, Universidad Nacional Autónoma de México, Blvd. Juriquilla No. 3001, C.P. 76230, Querétaro, México.

[2] School of Geosciences, University of South Florida, 4202 E. Fowler Avenue, C.P. 33620, Tampa, Florida, USA.

[3] Department of Geological Engineering and Science, Michigan Technological University, Houghton, Michigan, USA.

[a]lcapra@geociencias.unam.mx, [b]sylvain@usf.edu, [c]r.orozco@geociencias.unam.mx, [d]rpescoba@mtu.edu, [e]omar.cruzv@geociencias.unam.mx.

Corresponding author, [*]eduardpicor@geociencias.unam.mx.

Abstract

Atitlán stratovolcano, the fourth most hazardous volcano in Guatemala, has repeatedly generated lava flows, fallout deposits, and pyroclastic density currents (PDCs) during the Holocene, with PDC deposits extending up to 9 km from the summit. Approximately 80,000 inhabitants live within 10 km of the summit, mainly in Santiago Atitlán and San Lucas Tolimán municipalities, built over volcanic related deposits. This study presents the first probabilistic hazard assessment of PDCs at Atitlán, using depth–averaged numerical simulations within a Monte Carlo framework. Based on stratigraphic constraints, two end–member magnitude scenarios are defined: lower–volume (0.5–10 Mm^3) PDCs, confined within ravines, and higher–volume (10–100 Mm^3) PDCs that include a concentrated component, and an associated fine–grained layer able to spread beyond topographic barriers. Two complementary models are applied: *Titan2D*, simulating confined, friction–dominated flows, and *VolcFlow*, representing the PDC as two coupled layers (concentrated and dilute). Model inputs are constrained using field–derived mobility and volume estimates from four reconstructed PDC deposits; parameter uncertainty is explored via Latin Hypercube Sampling (300 simulations per source and volume range). Low–volume events produce channelized inundation with highest probabilities along the southern flank. High–volume scenarios produce broader inundation, with PDCs reaching the urban areas of Santiago Atitlán and San Lucas Tolimán, with maximum burial depths of 5–20 m in the populated sectors. These results provide

the first PDC probabilistic hazard assessment for Atitlán and constitute a foundational input for multi–hazard risk assessment and emergency planning in the Lake Atitlán basin.

Keywords: Pyroclastic density currents; Probabilistic hazard assessment; Titan2D; VolcFlow; Monte Carlo simulation; Atitlán volcano, Guatemala.

1. Introduction

Pyroclastic density currents (PDCs) are among the most destructive volcanic hazards, responsible for thousands of fatalities in recent eruptions worldwide (Brown et al., 2017), including Merapi in 2010 (Surono et al., 2012) and Fuego in 2018 (Charbonnier et al., 2023a). Central America is particularly vulnerable to these hazards, as its densely populated highlands are surrounded by numerous active stratovolcanoes (Ewert & Harpel, 2004). The most recent example of this vulnerability occurred on June 3rd, 2018, when Fuego volcano (Guatemala) generated small–volume PDCs that propagated more than 12 km and buried the community of San Miguel de Los Lotes, causing at least 430 confirmed fatalities, with the actual toll likely much higher (Charbonnier et al., 2023a). This event demonstrated the devastating impact that even small–volume PDCs (<30 Mm^3, Charbonnier et al., 2023a) can have in densely populated regions and underscored the need for improved hazard assessments.

In this context, Atitlán stratovolcano stands out as one of the most hazardous in Guatemala, ranked fourth among Guatemalan volcanoes in terms of hazard score yet first in all of Latin America in the Volcanic Risk Ranking (Guimarães et al., 2021) due to the low resilience of nearby communities. Population projections for 2026 estimate that approximately 80,000 people live within 10 km of the summit, with over 300,000 residing within the Lake Atitlán basin (AMSCLAE, 2018; INE, 2019). The towns of Santiago Atitlán and San Lucas Tolimán are particularly vulnerable, as they were partially built over volcanic related deposits, including PDCs (Haapala et al., 2005).

Atitlán Volcano is the youngest of the three stratovolcanoes (San Pedro, Tolimán, and Atitlán) developed around the southern rim of Atitlán Caldera (Newhall, 1987; Newhall et al., 1987; Penfield et al., 1986) following the most recent caldera–forming silicic eruption (~64 +/– 8 ka; Cisneros de León et al., 2025). Since the arrival of the Spaniards, at least five eruptive episodes have been documented (1469, 1524, 1706, 1717, 1826–1856; Montessus de Ballore, 1884; Sapper, 1925), and at least eleven eruptive cycles have occurred since the Mayan Preclassic period (~3080 ± 30 BP; Pico Rodriguez et al., 2026).

Most eruptions at Atitlán follow a recurring pattern: an initial fallout phase, followed by lava effusion and lava fountains and the subsequent generation of PDCs through gravitational collapse of lava flows and oversteepened

pyroclastic material near the summit and upper flanks. Atitlan products consists of fallout layers interbedded with both massive fine–grained PDC deposits and BAF deposits (Pico Rodriguez et al., 2026). These deposits occur on all flanks and extend up to 9 km from the crater to the base of the edifice, where present–day settlements and agricultural estates are located (Fig. 1).

Considering the high exposure of local populations and the destructive potential of PDCs, this study presents the first probabilistic hazard assessment of PDCs at Atitlán, using a Monte Carlo framework with the *Titan2D* and *VolcFlow* models to quantify PDC inundation areas and develop a probabilistic hazard map; a fundamental step toward a comprehensive multi–hazard evaluation of the volcano.

2. PDCs at Atitlán stratovolcano

Atitlán stratovolcano has predominantly generated PDC deposits through gravitational collapse of lava flows and oversteepened unconsolidated volcaniclastic material accumulated in the summit and upper flanks (Pico Rodriguez et al., 2026), a mechanism commonly observed at basaltic volcanoes (Andronico et al., 2018; Zuccarello et al., 2025). At least eleven eruptive cycles over the last ~3400 years have occurred at Atitlán, each comprising scoria fallout layers interbedded with PDC deposits as part of multiphase eruptive sequences (Pico Rodriguez et al., 2026). These deposits include: BAFs, characterized by massive, poorly sorted, block–rich units up to 20 m thick containing basalt–andesite lithic blocks up to 60 cm diameter; and fine–grained PDC deposits, represented by ash and fine lapilli rich layers that drape distal slopes (Fig. 2). The most distal preserved exposures –those farthest from the source – lie 4 to 9 km from the summit.

Although the footprints of most recent and historical PDC deposits cannot be reconstructed due to discontinuous and limited exposures, four events can be reliably traced laterally at multiple outcrops on the northern, northwestern, western, and southern flanks of the volcano (Fig. 1, Table 1). Radiocarbon ages of charcoal relate these deposits with two main eruptive periods: the northwestern and eastern PDC deposits originated during the Preclassic Mayan period (1421–1130 BC) whereas the western, southern, and some of the northern PDC deposits are associated with the last eruptive activity (1826–1856; Haapala et al., 2005; Pico Rodriguez et al., 2026).

The northwestern PDC deposits comprise five BAF units (Fig. 2A & 2B) exposed along the road to Santiago Atitlán, where two nearby quarries (<200 m apart) reveal a sequence up to 20 m thick located 4.2 km from the summit. The western PDC deposit consists of a highly weathered, fine–grained unit preserved along the summit trail, with

thicknesses between 0.2 and 1.5 m, and its most distal exposure is located 4.4 km from the summit. The southern flank contains the most distal PDCs, extending up to ~9 km from the summit. These include a BAF unit up to ~2 m thick and an associated fine–grained PDC deposit, ~0.26 m thick (Fig. 2C). The PDC deposit identified in the northern flank consists of a fine–grained unit, 0.4 to 1.5 m thick, with its most distal preserved exposure located ~3.8 km from the summit (Fig. 2D).

Since the reconstruction of past PDC deposit extent is limited by discontinuous and scattered outcrops, the inundation areas of the four PDC events considered (Fig. 1) are likely underestimated. Deposit volumes were estimated by multiplying the thickness measured at each preserved outcrop by the reconstructed inundation area of the corresponding PDC, yielding minimum and maximum estimates for each deposit. These values should be regarded as a range of uncertainty: minimum values may underestimate the actual deposit volume, whereas maximum values likely overestimate it.

3. Magnitude and extent of Atitlán PDCs

The magnitude, mobility, and extent of past PDCs at Atitlán were constrained using two parameters: the coefficient of friction ($\Delta H/L$) and the bulk deposit volume ($A \times T$). The coefficient of friction is defined as the ratio between the vertical drop of the flow (ΔH) and the horizontal runout distance (L), with lower values indicating more mobile currents (Ogburn & Calder, 2017 after Heim, 1932). Since the original flow fronts are not preserved, L is expressed in this work as the horizontal distance between the interpreted source and the most distal outcrops. Consequently, the resulting values represent minimum mobility estimates: the actual PDCs were likely more mobile.

Bulk deposit volumes were estimated by multiplying the reconstructed inundation areas (A) by the averaged deposit thicknesses (T) measured at key outcrops (see Table 1). Minimum and maximum values encompass the uncertainty introduced by erosion, incomplete exposures, and depositional variability of the PDC deposits. These metrics provide first–order estimates of PDC behavior and serve as benchmarks for calibration of the numerical simulations (Ogburn & Calder, 2017).

4. Numerical models

Titan2D and *VolcFlow* have been widely applied to PDC hazard assessments (Aravena et al., 2024; Charbonnier et al., 2020; Kelfoun et al., 2017) due to their practicality and relatively low computational cost compared

to fully three–dimensional multiphase models, making them suitable for probabilistic or scenario–based hazard assessments. Both models solve mass and momentum conservation equations in two horizontal dimensions by averaging flow properties (e.g., velocity, pressure, density) over flow thickness (Pitman et al., 2003; Kelfoun & Druitt, 2005). This *depth–averaged* approach neglects vertical variations but captures the essential dynamics of gravity–driven flows while preserving key physical processes such as acceleration and lateral spreading. Both models operate on a digital elevation model (DEM), that provides the topographic boundary conditions controlling flow motion (Patra et al., 2005; Kelfoun, 2017).

Despite sharing the same theoretical foundation, contrasting rheological formulations enable both models to reproduce complementary PDC dynamics. In this work, we used *Titan2D* with a frictional–turbulent rheology (*Voellmy–Salm law*; Voellmy, 1955; Salm, 1993; Pitman et al., 2003; Patra et al., 2005), whereas the two–phase version of *VolcFlow* (Kelfoun, 2017) is used with a constant retarding stress (CRS) rheology (Kelfoun & Druitt, 2005; Kelfoun, 2017). This dual approach enables the simulation of both confined, valley–directed BAF and unconfined, laterally spreading dilute currents (Gueugneau et al., 2019; Charbonnier et al., 2020; Aravena et al., 2024).

4.1. *Titan2D*

Titan2D numerical code solves the depth–averaged mass and momentum conservation equations using a finite–volume Godunov scheme (Pitman et al., 2003; Patra et al., 2005). The governing equations account for the effects of gravity, topography, and basal resistance represented by the *Voellmy–Salm rheology* (Voellmy, 1955; Salm, 1993). In this formulation, basal shear stress is expressed as the sum of two components: a *Coulomb friction term*, proportional to the normal stress through the basal friction coefficient (μ), and a *velocity–squared turbulent drag term* controlled by a turbulent friction coefficient (ξ). Together, these terms allow *Titan2D* to represent both basal frictional resistance and momentum loss associated with turbulent drag (Denlinger & Iverson, 2001; Patra et al., 2005).

The Coulomb friction term depends on local slope and flow thickness, making *Titan2D* sensitive to topographic curvature and flow confinement (Charbonnier et al., 2023b; Aravena et al., 2024). Channelized valleys and steep flanks enhance the downslope gravitational component while restricting lateral spreading, reproducing the directional, confined behavior typical of BAF, whereas the frictional–turbulent rheology promotes rapid energy dissipation and reduced spreading in open or low–relief regions (Ogburn & Calder, 2017). *Titan2D* outputs (flow thickness, velocity, extent) are post–processed to estimate maximum runout distances and affected areas.

4.2. *VolcFlow*

VolcFlow (Kelfoun & Druitt, 2005; Kelfoun, 2017) was developed to simulate both concentrated and dilute components of PDCs. Like *Titan2D*, it solves the depth–averaged mass and momentum equations; however, it represents PDCs as two dynamically coupled layers: a basal concentrated flow and an overlying dilute current (pyroclastic surge). The dynamics of each layer are governed by distinct rheological formulations. In the concentrated layer, basal resistance is expressed with a *constant retarding stress* (CRS) rheology, acting opposite to the direction of motion and independent of the local slope or normal load. An additional velocity–dependent turbulent term (a_1) accounts for energy dissipation. The dilute phase is governed separately by a turbulent drag coefficient (a_2) proportional to the square of the surge velocity (Kelfoun, 2017).

Because the dominant resistance term (CRS) is independent of local slope and normal load, *VolcFlow* can maintain mobility over gentle slopes and flat terrains. Furthermore, its two–layer formulation allows the dilute phase to detach from the concentrated flow and propagate independently, overtopping topographic barriers that would halt a single–phase model. The contrasting rheological formulations make the two models complementary: *Titan2D* captures confined, friction–dominated flows, whereas *VolcFlow* reproduces laterally spreading currents that may transition into dilute PDCs.

4.3. Model input parameters.

Both *Titan2D* and *VolcFlow* require as input a DEM, source geometry and location, volume, and running time (Pitman et al., 2003; Kelfoun & Druitt, 2005). The source defines the area used by the model to introduce the material into the numerical domain, while the flow volume controls the overall magnitude of the event. The simulation duration (running time) was set sufficiently long to allow complete flow emplacement and stabilization. Since neither model produces complete flow rest, a minimum velocity threshold of 1–2 m s^{-1} was used to define flow arrest in both Titan2D and VolcFlow simulations.

All numerical simulations were performed using a DEM of Atitlán volcano with a spatial resolution of 12.5 m, derived from ALOS PALSAR data. The DEM was obtained from the Alaska Satellite Facility data portal (ASF DAAC, 2014).

In *Titan2D*, material supply uses a flux–source formulation, where influx rate (F) depends on total volume (V), circular source radius (r) and influx time (t_1) (Patel et al., 2022). Influx rate (F) describes the volumetric rate of material injected into the model domain. This relationship is expressed as:

$$F = \frac{4V}{\pi r^2 t_1}$$

Titan2D additionally requires the rheological parameters μ and ξ (Patra et al., 2005; Patra et al., 2023). The basal friction coefficient (μ) is a dimensionless parameter that controls the overall mobility of the current and is defined as:

$$\mu = \tan \varphi,$$

where φ is the basal friction angle ($\mu \geq 0$). Lower μ values (0.05–0.2; $\varphi \approx 3°–11°$) produce more mobile flows with longer runouts; whereas higher μ values (>0.4; $\varphi > 22°$) increase basal resistance and result in less mobile flows with shorter runouts (Patra et al., 2005; Ogburn & Calder, 2017).

The turbulent drag coefficient (ξ) used in *Titan2D* represents the dissipation of energy due to internal turbulence and is expressed as a velocity–squared term, with units of m s^{-2}. Calibrations in Voellmy–type applications commonly employ ξ values between 10^2–10^3 m s^{-2} for dry granular and snow–avalanche analogs (Fischer et al., 2012; de' Michieli Vitturi et al., 2019).

In *VolcFlow*, the total flow volume is imposed as an initial condition, spatially distributed within the prescribed source geometry. Flow resistance is governed by three parameters: the constant retarding stress (CRS), expressed in pascals, which controls the mobility of the concentrated flow independently of local slope; a dimensionless turbulent coefficient a_1, which accounts for velocity–dependent energy dissipation in the concentrated flow; and a turbulent drag coefficient a_2, which governs resistance in the dilute phase (Kelfoun, 2017). In this study, a_1 was fixed at 0.01 and a_2 at 0.05 for all simulations , while CRS varied in the Monte Carlo ensemble. Published calibrations for small–to–moderate PDCs employ CRS values that range from a few to several tens of kPa; including ~2–50 kPa at Soufrière Hills Volcano (Ogburn & Calder, 2017) and 3–10 kPa at Merapi volcano (Charbonnier et al., 2023b).

4.4. Source conditions

To represent potential source locations of PDC initiation, the summit region was divided into four circular sources with a radius of 55 m, positioned along the crater rim and oriented toward the southern, western, northern,

and northeastern flanks of the volcano (Fig. 3). Each source defines the location where the already–mobilized volume is released. The 55 m radius was selected based on preliminary stability tests, as larger source areas produced numerical instabilities in *Titan2D* under the adopted extent and DEM spatial resolution. The southern source was used during model calibration, whereas the full set of source locations was employed in the subsequent probabilistic simulations.

The current crater of Atitlán stratovolcano has a diameter of ~185 m and is open toward the south, where the rim reaches its lowest elevation. The highest summit elevation occurs toward the northeast, where a paleocrater forms a local topographic high (Fig. 3) that is partially infilled by recent lava flows (Pico Rodriguez et al., 2026). These flows remained largely confined within the paleodepression and only overtopped the paleorim toward the northern sector. No recent lava flows extend toward the eastern flank, although older lava flows are present in that sector (Pico Rodriguez et al., 2026).

The area east of the modern crater lies at a lower relative elevation and has steeper slopes than the paleostructure. Therefore, a source located east of the crater would initiate within a confined sector, favoring gravitational deflection toward the S–SE sector. To represent collapse directions compatible with potential eastern–flank propagation under the present morphology, a northeastern source positioned on the paleocrater was therefore included among the modeled scenarios (Fig. 3).

For *VolcFlow* probabilistic simulations, a single circular source centered on the main crater was defined. The diameter (319 m) was constrained to encompass and intersect the *Titan2D* source areas, ensuring spatial consistency in the initial conditions across both models. The simplified source conditions adopted for both models, do not resolve the PDC generation mechanism; instead they provide generalized initial conditions independent of the process that triggered the formation of the PDCs.

4.5. Model calibration

Model calibration aimed to identify rheological parameter ranges (μ and CRS) capable of reproducing the extent and runout of the best–constrained PDC deposits at Atitlán. For calibration purposes, non–rheological source parameters (total flow volume, running time, and source geometry) were fixed according to the values summarized in Table 2. To ensure consistency between models, calibration runs were performed using a circular source with a radius of 55 m, south of the crater (Fig. 3). This source corresponds to one of the summit–oriented vents defined in Section

4.4 and was selected because it aligns with the direction of the longest preserved PDC deposit runouts at Atitlán. The remaining summit source locations were excluded from the calibration phase and were only considered in the subsequent probabilistic simulations.

4.5.1. Titan2D input parameters

To limit computational complexity while maintaining physical accuracy, the turbulent drag coefficient (ξ) was fixed at 300 m s^{-2} and only the basal friction coefficient (μ) was varied. Simultaneously sampling both μ and ξ within a probabilistic framework would exponentially increase the number of simulations required, making modeling computationally prohibitive. Previous sensitivity analyses have shown that μ exerts the dominant control on the overall mobility and runout of PDCs, whereas ξ primarily influences high–velocity dissipation during the later stages of flow deceleration (Aravena et al., 2024; Charbonnier et al., 2020; Patra et al., 2005). Fixing ξ therefore isolates the influence of basal friction while retaining a realistic representation of turbulent energy loss, providing a balance between physical accuracy and computational feasibility. A relatively low value of ξ (300 m s^{-2}) was selected here to avoid excessive turbulent dissipation and to ensure that the basal friction coefficient (μ) remains the principal parameter controlling current mobility.

Basal friction coefficient (μ) values were varied from 0.05 to 0.5 in increments of 0.025 (Table 2). This is consistent with previous *Titan2D* applications for BAFs at Merapi (Charbonnier & Gertisser, 2009). Low μ values (<0.2) favor highly mobile flows while higher μ values (0.3–0.4) promote earlier deceleration and shorter runouts. This range captures the frictional conditions required to reproduce the long southern BAF deposit runouts and the smaller western and northern BAF deposits observed at Atitlán. Influx time and the corresponding influx rate were prescribed consistently with the selected volume and source geometry.

4.5.2. VolcFlow input parameters

Constant retarding stress (CRS) values used range between 2 and 10 kPa in increments of 500 Pa each. This is consistent with prior *VolcFlow* calibrations for PDCs at Merapi volcano (Charbonnier et al., 2023b). Lower CRS values (2–5 kPa) favor more mobile flows with greater lateral spreading, similar to fine–grained PDC deposits found on the southern flank of Atitlán. Higher values (6–9 kPa) increase basal resistance and produce shorter runouts and

thicker deposits. A similarly low value of the turbulent friction coefficient ξ (300 m s^{-2}) as for *Titan2D* was selected for consistency.

4.5.3. Modeled and observed PDC deposits

Titan2D and *VolcFlow* calibration simulations were compared against the selected observed PDC deposits to evaluate if the adopted rheological parameter values were capable of reproducing their footprints (Fig. 4). This calibration step constrained the ranges of the input parameters used for the Monte Carlo simulations.

4.6. Monte Carlo analysis and parameter sampling

Field–derived constraints from the observed deposits were integrated into a probabilistic hazard assessment based on a Monte Carlo framework. Instead of relying on a single deterministic scenario, input parameters (volume, rheology, and source location) are randomly sampled from predefined ranges, and each sampled parameter set is used to generate an independent model realization. The resulting ensemble explores physically admissible combinations of eruptive volume, rheological parameters, and source conditions, and is aggregated to derive spatial probabilities of PDC inundation, providing a quantitative representation of hazard that accounts for both natural and epistemic uncertainty (Ogburn & Calder, 2017).

Parameter sampling for the Monte Carlo analysis was performed using a Latin Hypercube Sampling (LHS) strategy (McKay et al., 1979). This method provides a more uniform and efficient coverage of multidimensional parameter space with a limited ensemble size (300 simulations per source and volume scenario; see Section 5.1; Helton & Davis, 2003; Fig. S1).

Potential correlations between sampled parameters were addressed differently for each scenario. For the lower–volume scenario (Titan2D), μ was conditioned on volume through a rejection scheme: samples were retained only if they fell within the prediction bounds of the calibrated volume–mobility relationship for BAFs. This imposes the inverse correlation between volume and ΔH/L (Heim, 1932; Ogburn & Calder, 2017). For the higher-volume scenario (VolcFlow), CRS was sampled uniformly within the calibrated range (2–10 kPa) without volume conditioning, as its relative effect on mobility varies with flow thickness through the model formulation.

5. Results

5.1. Reference volume scenarios and probabilistic framework

Bulk volumes of individual PDC deposits at Atitlán range from 0.42 to 63 Mm^3 (Table 1), consistent with eruptive activity spanning from strombolian to sub–plinian intensity (VEI 3–4; Pico Rodriguez et al., 2026). To encompass this range while accounting for uncertainties related to erosion, incomplete exposure, and potential underestimation of distal deposits, three reference volume scenarios were defined for the model calibration: 1, 10, and 100 Mm^3. For the Monte Carlo analysis, these reference volumes were grouped into two end–member ranges: (i) a lower–volume scenario (0.5–10 Mm^3), consistent with the preserved PDC deposits on the northern and western flanks, and (ii) a higher–volume scenario (10–100 Mm^3), consistent with the deposits on the southern and northwestern flanks (Table 1). The scenarios adopted here (lower and higher volumes) are relative to the magnitude of the PDCs generated by Atitlán volcano. In the broader literature, both scenarios fall within the range of small to intermediate PDCs (Charbonnier et al., 2023a).

For each source location and volume range (0.5–10 Mm^3 & 10–100 Mm^3), an ensemble of 300 simulations was generated. This ensemble size represents a compromise between computational feasibility and statistical robustness and is sufficient to produce stable spatial patterns of inundation when a LHS method is employed (Charbonnier et al., 2020; Ogburn & Calder, 2017). Results are presented in two parts: (i) calibration outcomes and consistency with field–based constraints, and (ii) probabilistic inundation patterns and maximum thickness distribution.

5.2. Calibration outcomes and consistency with field–based constraints

Calibration aimed to evaluate whether the rheological parameter ranges adopted were capable of reproducing the mobility and deposit characteristics of the two end–member PDC types documented at Atitlán: confined BAFs, modeled with *Titan2D*, and high–volume PDCs with associated fine–grained facies, modeled with *VolcFlow*. Simulations were conducted under fixed source conditions and variable rheological parameters (Table 2), and compared against field–derived volume and mobility estimates (Figure 4).

For both models, the ensemble of calibrated simulations spans the range of mobility inferred from field data, with modeled deposit volumes and $\Delta H/L$ values overlapping those derived from the stratigraphic record (Figure 4). For the largest–volume calibration scenario (100 Mm^3), four *Titan2D* simulations corresponding to the lowest basal

friction coefficients ($\mu \leq 0.125$) extended beyond the DEM and did not return valid outputs. Therefore, the *Titan2D* interdecile range (Figure 4; shaded envelope) is narrower for this volume. Despite this limitation, *Titan2D* produces a broader mobility range ($\Delta H/L$) than *VolcFlow*, reflecting its stronger sensitivity to variations in basal friction coefficient. *VolcFlow* produces a narrower mobility range because the CRS formulation is sensitive to flow thickness variations, which remain limited under the small–volume BAF conditions modeled here.

Although field constraints for the largest PDC volumes at Atitlán remain limited, the higher–volume scenario falls near the P10–P90 mobility range defined for *VolcFlow*. This provides a closer match to the mobility of the most voluminous and distal deposits preserved on the southern flank. These deposits include BAFs and associated fine–grained facies, emplaced across gentler slopes and less confined topography (Pico Rodriguez et al., 2026). Therefore, *Titan2D* was used for the lower-volume scenario (0.5–10 Mm^3), where flow propagation is strongly controlled by steep slopes and channelized topography, whereas *VolcFlow* was used for the higher–volume scenario (10–100 Mm^3), where the dilute component contributes in the transport dynamics, particularly when topographic confinement drops.

5.3. Probabilistic inundation patterns: lower–volume scenario (0.5–10 Mm^3)

Probabilistic inundation maps for the lower–volume scenario integrate the results from the four summit–oriented source locations (west, south, north, and northeast; Fig. 3), with 300 *Titan2D* simulations per source. The resulting inundation footprints were combined into a single conditional probability map (Fig. 5).

Inundation probability was calculated as the fraction of simulations in which flow thickness exceeded 0.05 m. Non–informative simulations were excluded, resulting in slightly different numbers of realizations per sources (Fig. 5), but remains in the order of 300 realizations per source.

Results indicate that inundation is mostly confined to proximal and intermediate sectors. Near the summit, all flanks are inundated with the highest probabilities concentrated on the southern flank. Downslope, simulated PDCs preferentially propagate along steep slopes and pre–existing channels, producing elongated inundation patterns within gullies and ravines. Probability values decrease rapidly downslope, and distal low–gradient areas exhibit negligible inundation (<5%, Fig. 5).

5.4. Probabilistic inundation patterns: higher–volume scenarios (10–100 Mm^3)

The higher–volume scenario was simulated using *VolcFlow*. Conditional probability of inundation was computed using the maximum flow thickness recorded at any timestep, using a minimum thickness threshold of 0.01 m (Fig. 6). Each simulation produces a footprint for the concentrated and dilute phases of the PDC. The conditional probability integrates the contribution of both phases and captures whether the flow reached a given cell during emplacement.

The probability map shows a markedly broader spatial extent than that observed for the lower–volume scenario. High probability zones (>0.5) extend across large portions of the NW, SW, and SE flanks, where flows propagate over smoother topography with substantial lateral spreading.

Probability decay with distance from the summit is more gradual than in *Titan2D* simulations. Distal sectors retain moderate exceedance probabilities, and simulated flows even reach the shoreline of Lake Atitlán, where the municipality of Santiago Atitlán is located. In contrast, the eastern flank remains comparatively less affected with flows predominantly diverted toward the northern and southern sectors by the presence of the paleocrater.

5.5. Maximum thickness distribution: lower–volume scenario (0.5–10 Mm³)

Maximum flow thickness maps were computed by extracting, at each grid cell, the highest simulated thickness (Fig. 7). The resulting map shows that significant accumulation (>2 m) occurs primarily within the summit region, along confined channels and slope breaks where flow deceleration promotes material accumulation. Outside these corridors, thickness rapidly decreases, and interfluves remain largely unaffected. The highest thickness values are observed on the southern flank where a ravine redirects the PDCs through the southwest, where they reach up to 30 m thick.

In contrast to probabilistic maps, which quantify likelihood, the maximum thickness map represents an upper–bound scenario within the calibrated parameter ranges. These values should therefore be interpreted as extreme but physically admissible outcomes.

5.6. Maximum thickness distribution: high–volume scenario (10–100 Mm³)

Maximum deposit thickness maps were derived independently for the concentrated and dilute phases of the PDCs simulated from the *VolcFlow* ensemble by accounting, for each grid cell, the highest value across all simulations

(Fig. 8). The combined map integrates both phases and reveals a clear spatial transition in the dominant depositional process between proximal and distal sectors.

Proximal and intermediate sectors are dominated by the dilute–phase deposits, covering a broad area of the volcanic edifice with maximum thicknesses of 2–5 m. The concentrated–phase deposits in this sector are spatially more restricted and generally thinner (<2m). In distal sectors, the pattern reverses, the concentrated–phase becomes the dominant contributor to maximum thickness. This spatial distribution reflects the strong topographic control exerted by the drainage network. On the southern, southeastern, southwestern, and western flanks, flow propagation follows a well–defined dendritic pattern controlled by deep ravines. The deeply incised canyons on the WSW flank fully confine flows, producing the thickest deposits (>30 m). On the southwestern and southeastern flanks, where topography smooths out, distal flows spread laterally beyond channel margins, producing broader and thinner footprints (5–20 m).

6. Discussion

6.1. Model calibration outcomes and best–fitting input parameters

Calibration of *Titan2D* and *VolcFlow* models indicate that both reproduce first–order mobility characteristics of past PDCs at Atitlán. Modeled outcomes overlap with the observed deposit–derived mobility ranges (Fig. 4), indicating that the selected rheological parameter spaces are physically admissible and consistent with the stratigraphic record.

Both models were calibrated against PDC deposits interpreted as products of gravitational collapse of lava flows, the mechanism inferred to dominate PDC generation at Atitlán from the stratigraphic record. The differentiation between models is based on rheological compatibility with field–derived mobility constraints at each volume range: *Titan2D* better reproduces the confined, friction–dominated dynamics of lower–volume BAFs, whereas *VolcFlow*'s two–layer formulation captures the lateral spreading associated with larger–volume events where an ash–cloud surge component becomes significant.

6.2. *Titan2D* and *VolcFlow* behavior differences

The contrasting spatial patterns observed between the two scenarios (Fig. 5 and 7) reflect differences in rheological formulation, volume interval, and modelling approach. In the lower–volume scenario, *Titan2D* produces inundation patterns strongly constrained by topography: basal resistance scales with the effective normal stress,

leading to rapid deceleration on low–gradient surfaces and limited overspill across interfluves (Patra et al., 2005; Pitman et al., 2003). This results in probabilistic maps with elongated, valley–confined patterns, where probability decays rapidly with distance from the summit. Similar patterns have been documented in comparative modeling studies of dense PDC undercurrents at Soufrière Hills Volcano (Ogburn & Calder, 2017).

In contrast, the higher–volume scenario simulated with *VolcFlow* exhibits broader spatial spreading and a more gradual decay of probability with distance (Fig. 6). This behavior is primarily controlled by the CRS and the two–phase modeling formulation, which allows the dilute phase to detach from the concentrated flow and propagate independently across topographic barriers (Kelfoun, 2017), a behavior absent in single–phase models like *Titan2D*.

Differences between both scenarios can be further assessed using the mobility ratio ($A/V^{2/3}$; Fig. 9 and 10), which quantifies lateral spreading relative to flow volume (Iverson et al., 1998; Charbonnier et al., 2013). Higher values indicate broader, less confined PDCs, whereas lower values correspond to thicker, more confined flows. Across both models, the mobility ratio is strongly influenced by the rheological parameters: higher basal friction (μ) in *Titan2D* and higher constant retarding stress (CRS) in *VolcFlow* both produce smaller, more confined flows (warmer colors in Fig. 9 and 10).

The mobility ratio for the four *Titan2D* simulations reveals a volume–dependent pattern. The ratio rises steeply at low volumes, reaches a maximum, and then declines or plateaus once the available confining topography becomes filled (Fig. 9); the turnover volume is sector–dependent. In the eastern source, the ratio increases across the entire simulated range (0.5–10 Mm^3), indicating that PDCs continue to overspill and gain area as volume grows. In the northern source, the ratio peaks near 2 Mm^3 and declines gently thereafter, whereas in the southern source it decreases sharply below ~4 Mm^3 and then flattens. The western source shows a weak, scattered increase. This progression is consistent with a process of topographic saturation: at low volumes, flows widen rapidly as they reach channel margins, but once the available confining topography is filled, additional volume preferentially thickens the deposit rather than expanding its footprint. The turnover volume therefore reflects the confining capacity of each flank. This control is also expressed in the mean mobility ratios, which increase from the deeply incised southern drainages (202) through the eastern (227) and western (274) flanks to the more open northern sector (374), tracing a gradient of decreasing topographic confinement.

The higher–volume *VolcFlow* simulations (10–100 Mm^3) reflect the same saturation behavior: since this range lies entirely above the volume-saturation threshold, added volume is accommodated by increasing deposit

thickness rather than lateral extent, producing deep accumulation zones (Fig. 8 and 10) and a mobility ratio that decreases throughout the range (Fig. 10). The greater scatter at equivalent volumes and CRS values reflects the stronger role of local topography in redistributing large flows across the summit region. Under these conditions, intermediate slopes accumulate substantial material, and distal low–gradient areas that remained largely unaffected in the lower–volume scenario now show measurable deposition (Fig. 8 and 10), with the southeastern and southwestern flanks being the most heavily impacted. The higher mean mobility ratio of the *VolcFlow* simulations (423) relative to Titan2D (267) is consistent with the greater lateral mobility of larger flows, although the two ranges cannot be compared directly because they span different volumes.

Interpreted together, the two models describe a single continuum of PDC behavior, expressed by the mobility ratio: from confinement–limited spreading to thickness–dominated accumulation. This continuum reflects the complementary strengths of the two models: the friction–dominated, valley–confined dynamics of BAFs in Titan2D, and the capacity of VolcFlow to capture the decoupled dilute phase able to exceed topographic barriers. Similar contrasts have been reported in benchmarking and comparative modeling studies (Gueugneau et al., 2021; Ogburn & Calder, 2017). Considering both approaches as complementary provides a more robust representation of the range of PDC processes expected at Atitlán.

6.3. Effect of topography on PDC propagation and inundation patterns

Topography exerts a first–order control on PDC propagation under both scenarios, although its relative influence decreases as volume increases. In the lower–volume scenario, drainage networks dictate flow direction and accumulation zones. The southern source consistently produces the lowest mobility ratios (Fig. 9), reflecting strong channelization by deeply incised canyons, whereas the northern source produces the highest mobility ratios. Maximum thickness maps (Fig. 7 and 8) show localized accumulation within ravines and at slope breaks, consistent with the strong influence of topographic confinement. This valley–confined behavior can be observed in depth–averaged simulations of BAFs at stratovolcanoes such as Stromboli and Merapi (Salvatici et al., 2016; Charbonnier et al., 2023b).

Under higher–volume conditions, topographic control remains evident but becomes less restrictive. Major valleys guide the concentrated phase (Fig. 8), whereas the two–phase formulation allows the dilute phase to spread across smoother terrain. Southeast of the crater, for example, a prominent scarp redirects the lower–volume PDCs

(Fig. 5) whereas the higher–volume flows surpass this topographic barrier. The northern and northwestern flanks, which are less dissected, show broader inundation patterns in both models, covering most of the flanks without a clear dendritic pattern.

The paleocrater northeast of the current summit provides an additional additional topographic control. In the higher–volume *VolcFlow* simulations, PDCs are preferentially diverted toward the northern and southern sectors, leaving the eastern flank comparatively less affected. In contrast, the lower–volume *Titan2D* simulations include a northeastern source within the paleocrater to assess potential PDC propagation toward the eastern flank. This contrast highlights the role of the paleostructure in present–day flow routing. Considering the presence of preserved BAF deposits on the eastern flank dated to ~3 ka BP (Haapala et al., 2005), suggests that the paleocrater either did not exist at that time or, more likely, functioned as the principal vent. Under the present topographic configuration, PDCs generated at the current crater tend to be deflected away from the eastern flank in the higher–volume simulations; however, this deflection is conditional on the current morphology and on the modelled summit sources, and should not be interpreted as intrinsic protection of eastern–flank communities.

To explore a hypothetical scenario in which an abrupt or gradual change in the current summit morphology — such as intense or periodic lava extrusion — favors PDC generation toward the northeastern flank, a deterministic simulation was performed with *Titan2D* from the same northeastern source used in the probabilistic ensemble, but with a higher reference volume of 25 Mm^3, comparable in magnitude to the 2018 Fuego PDCs that affected the *Las Lajas* ravine (Charbonnier et al., 2023a). The basal friction coefficient for this scenario was varied across the range predicted by the volume–mobility relationship for this volume (μ = 0.06–0.18). The inundation envelope across these seven runs is reported using the same 0.05 m thickness threshold applied previously (Fig. 11, dotted polygon; Fig. S2).

Results show that the simulated PDC reaches the villages, communities, and *fincas* located at the base of the eastern flank, with a maximum runout distance of ~7 km from the source (Fig. 11, dotted polygon). The footprint also extends to the southern urban area of San Lucas Tolimán. The resulting deposit reaches 5–20 m thick at the flow front, burying the eastern settlements. Since the main access road would also be buried in this event, this scenario represents a hazard that should be considered in evacuation planning and mitigation strategies for the eastern sector.

6.4. Maximum thickness patterns and impact severity

Beyond spatial probability, the maximum–thickness maps provide critical information regarding impact intensity. While probability maps constrain likelihood of inundation, thickness envelopes constrain potential destructive capacity.

For the lower–volume *Titan2D* scenario, maximum thickness remains spatially restricted and strongly aligned with valley axes (Fig. 7). Localized peaks occur within steep ravines and slope breaks, but accumulation rapidly decreases outside confined channels. In contrast, the higher–volume *VolcFlow* scenario (Fig. 8) produces both expanded footprints and substantially greater maximum thicknesses for the concentrated phase, with values exceeding several tens of meters in proximal and intermediate sectors.

The spatial distribution of maximum thickness does not directly mirror probability patterns. Certain sectors may exhibit moderate inundation probability but high envelope thickness, indicating low–frequency yet high–severity outcomes. This distinction is critical for hazard assessment, as infrastructure vulnerability is strongly dependent on deposit thickness and dynamic loading.

The southeastern, southwestern, and northwestern flanks consistently exhibit both elevated probabilities and high maximum thickness under the high–volume scenario, identifying them as sectors of compounded hazard. Conversely, the eastern flank, although less affected in the high–volume simulations due to the paleostructural diversion, remains susceptible under the lower–volume *Titan2D* scenario. Moreover, a morphological change of the crater could enable eastward propagation of higher–volume PDCs, as shown by the paleocrater scenario in Section 6.3, which reaches inhabited areas on the eastern flank.

Integrating probability and maximum thickness maps provides a two–dimensional hazard characterization: likelihood of occurrence and potential severity. This combined framework aligns with scenario–based probabilistic approaches applied to PDC hazard assessment at Aluto and Tungurahua (Aravena et al., 2024; Clarke et al., 2020).

6.5. Hazard implications and potential future scenarios

The maximum inundation limits of PDCs for both scenarios acquire practical relevance when evaluated in the context of the demographic distribution (Fig. 11). The most populated municipalities in the immediate vicinity are Santiago Atitlán (northwest flank) and San Lucas Tolimán (northeast flank). Several agricultural estates and rural communities largely occupy the southern and eastern flanks.

According to the 2018 census, the municipality of San Lucas Tolimán had 29,772 inhabitants and Santiago Atitlán 41,877 (INE, 2019). Population projections from the National Institute of Statistics (INE, 2019) estimate that by 2026 these values increase to 32,084 and 49,083 inhabitants, respectively. Although detailed demographic data for individual rural communities are limited, the village of *El Esfuerzo* alone was estimated to host approximately 2,280 inhabitants in 2021, indicating non–negligible exposure in the southern flank. Several additional settlements and agricultural estates are distributed along the southern and eastern flanks, including the *fincas Moca Grande*, *Olas de Moca*, *Asunción*, *Los Andes Natural Reserve*, *Florencia*, *Los Tarrales*, and *Pampolija*, as well as the villages *Las Ilusiones*, *El Esfuerzo*, *El Carmen*, *Santa Cruz Quixayá*, *Santa Teresa*, and *Panimaquip* (Fig. 11).

Lower–volume scenario (Titan2D, 0.5–10 Mm^3)

The lower–volume scenario produces spatially confined flows. Toward the eastern flank, inundation reaches the southern administrative boundary of San Lucas Tolimán and approaches the vicinities of *Panimaquip* and *Santa Teresa*. On the southern flank, inundation extends to *Finca Los Andes* and approaches *Finca Moca Grande*. To the northwest, flows reach the main access road to Santiago Atitlán and stops a few hundred meters from the urban boundary (Fig. 11).

Conditional probabilities of inundation in these sectors range between 0.05 and 0.2 (Fig. 5), with some portions of the southern flank locally reaching probabilities between 0.2 and 0.4. Maximum thickness values in inhabited sectors remain generally between 5 and 10 m within confined channels, decreasing rapidly outside drainage axes (Fig. 7). These results indicate that low–volume PDCs pose localized but significant hazard to agricultural estates, transport infrastructure, and peripheral settlements, particularly along valley corridors. Direct impact on densely urbanized sectors of Santiago Atitlán is limited under this scenario.

Higher–volume scenario (VolcFlow, 10–100 Mm^3)

The higher–volume scenario substantially increases both spatial extent and impact intensity (Fig. 11). To the northwest, inundation reaches Lake Atitlán and crosses portions of the urban area of Santiago Atitlán. The probability of inundation within northwestern municipal sectors remains generally below 0.6 (Fig. 6), while the probability of flows reaching the lakeshore is below 0.05. The main road connecting Santiago Atitlán shows probabilities between 0.6 and 0.8.

On the southern flank, *Fincas Olas de Moca, Moca Grande,* and *Los Andes* exhibit probabilities exceeding 0.6. The villages of *El Esfuerzo* and *Las Ilusiones* show probabilities between 0.2 and 0.6, whereas *El Carmen* remains below 0.05. Toward the southeast, *Finca Los Tarrales* shows probabilities exceeding 0.8, while *Finca Florencia* remains below 0.05. The scenario also intersects the main roadway connecting San Lucas Tolimán with a probability below 0.6 (Fig. 6).

Maximum thickness for the concentrated phase obtained in populated sectors under this scenario ranges between 5 and 20 m (Fig. 8). Such burial depths imply severe structural damage within inundated zones. Even where probability is moderate, envelope thickness values imply significant potential impact. Inundated sectors under the lower–magnitude scenario (Fig. 7) exhibit lower expected flow thickness, but could represent life–threatening conditions due to dynamic loading and thermal effects (Baxter, 1990; Valentine, 1998).

Potential impact therefore differs markedly between scenarios. Under low–volume events, impact is concentrated in confined valleys and peripheral infrastructure. Under high–volume conditions, impact extends to major population centers and critical transportation routes, including parts of Santiago Atitlán and southern rural communities.

Implications for risk management

The southern and southwestern flanks consistently emerge as the most exposed sectors due to the combination of high inundation probabilities and large maximum thickness values. The eastern flank remains partially shielded in the high–volume scenario by paleotopographic deflection but remains vulnerable under the lower–volume scenario and under the paleocrater scenario discussed above.

Given projected population growth toward 2026, exposure is increasing in both Santiago Atitlán and San Lucas Tolimán. Urban expansion toward drainage outlets and transportation corridors may further amplify vulnerability. These results emphasize the need for:

- Land–use regulation in high–probability corridors.
- Evacuation planning accounting for both confined and laterally spreading flow scenarios, and infrastructure design that recognizes potential burial depths exceeding 10 m under extreme conditions.

Frequency considerations and geological context

555 The two modeled scenarios represent distinct PDC volume end–members but do not imply different recurrence
556 probabilities. Because eruptive frequency for these volume classes has not been quantitatively constrained, both
557 scenarios must be treated as equally plausible conditional hazard states rather than ranked by likelihood.
558 Geological evidence introduces additional uncertainty in the interpretation of eastern–flank hazard. BAF deposits are
559 preserved on the eastern flank near currently inhabited areas and have been associated with Preclassic eruptive activity
560 (~3 ka BP, Haapala et al., 2005). These deposits indicate that the eastern flank was impacted by PDCs in the past,
561 under vent configurations or summit morphologies that may have differed substantially from the present. Their
562 absence from the probabilistic maps does not contradict this record: the probabilistic analysis is conditional on the
563 present summit morphology and source configuration, and is not intended to reproduce past events that occurred under
564 different conditions.
565 This distinction is supported by the modeling results themselves. In the deterministic northeastern scenario, even when
566 the source is deliberately placed on the paleocrater high to force eastward propagation, the present topography redirects
567 part of the flow toward the southern and northwestern flanks (Fig. S2). Moreover, the higher–volume *VolcFlow*
568 simulations — the least sensitive to topographic confinement — do not reach the eastern flank under the central source
569 configuration. Together, these results indicate that, under the present morphology, the eastern flank is not a natural
570 PDC travel path generated at the current summit area. The preserved eastern–flank deposits therefore most likely
571 record events sourced from a different vent, from the paleocrater when it functioned as the principal vent, or under a
572 summit morphology in which the present northeastern topographic high had not yet developed.
573 The present high–volume simulations consequently depict the eastern flank as comparatively less affected, a result
574 that reflects current topographic conditions, not an inherent reduction in hazard potential. This discrepancy highlights
575 two key uncertainties: potential changes in summit morphology through time, and sensitivity of flow routing to vent
576 location and paleotopography. Eastern–flank communities should therefore not be considered inherently protected
577 solely on the basis of current model outputs.
578 Taken together, the modeling results indicate that low–volume events (0.5–10 Mm^3) primarily threaten
579 confined drainage networks and proximal infrastructure; large–volume events (10–100 Mm^3) are capable of affecting
580 multiple populated sectors across the northwest, south, and southeast flanks; southern agricultural estates and rural
581 communities consistently show elevated potential impact under both scenarios; and the municipality of Santiago
582 Atitlán faces limited but non–negligible conditional impact under high–volume conditions (≥10 Mm^3).

583

584 **6.6. Multi–hazard context at Atitlán.**

585 Haapala et al. (2005) provides volcano–hazard–zonation maps covering lahars, tephra–fall, pyroclastic–flows
586 and lava–flows. In that work, the PDC and lava flow impact area are merged and represented as a line around the
587 volcano based on field observations. While those products offered an essential first–order multi–hazard baseline for
588 land–use planning, they were not designed to quantify conditional probabilities of inundation for PDCs under
589 uncertainty. This work therefore complements Haapala et al. (2005) by adding a probabilistic component for PDC
590 inundation based on depth–averaged numerical modeling and Monte Carlo sampling.

591 The combined use of (i) lahar zonation and (ii) tephra–fall scenarios from Haapala et al. (2005), together with
592 (iii) our conditional PDC probability and maximum–thickness maps, enables a more refined multi–hazard
593 prioritization around Lake Atitlán. Sectors with moderate PDC inundation probability (0.2–0.6) but high maximum
594 thickness (>10 m) represent high–severity outcomes that may be underestimated by zonation–based products, while
595 lahar corridors identified by Haapala et al. (2005) remain critical for post–eruptive rainfall remobilization even when
596 PDC inundation probability is low. This integration supports staged emergency planning –evacuation and road
597 management during eruptive crises, and lahar preparedness during subsequent rainy seasons– and highlights the need
598 for consistent hazard communication across processes and timescales.

599

600 **7. Conclusions**

601 This study presents the first probabilistic hazard assessment of PDCs at Atitlán stratovolcano, integrating
602 field–based constraints from preserved PDC deposits with depth–averaged numerical simulations in a Monte Carlo
603 framework. Both models were calibrated against PDC deposits interpreted as products of gravitational collapse of lava
604 flows, the mechanism inferred to dominate PDC generation at Atitlán from the stratigraphic record. Neither model
605 simulates PDC generation mechanisms — both assume that the current has already formed at the source and simulate
606 its subsequent propagation over the topography. *Titan2D* reproduces valley–confined mobilities typical of lower–
607 volume concentrated PDCs, whereas the two–phase version of *VolcFlow* simulates laterally spreading, higher–volume
608 currents where the dilute phase plays a critical role in determining the spatial extent of inundation.

609 Probabilistic inundation patterns differ systematically by volume class. For the lower–volume scenario (0.5–
610 10 Mm^3; *Titan2D*), inundation probabilities concentrate in proximal sectors and along channel networks, with rapid

probability decay downslope and limited interfluve overspill. For the higher–volume scenario (10–100 Mm^3; *VolcFlow*), probability fields broaden substantially, probability decay is more gradual, and inundation can extend to distal sectors including parts of the Lake Atitlán shoreline.

Maximum thickness maps add a severity dimension not captured by probability alone. In proximal and intermediate sectors, surge deposit thickness reaches 2–5 m over broad areas, while concentrated–phase deposits in distal channelized corridors attain 5–20 m, locally exceeding 30 m in deeply incised canyons on the southwestern flank. These thickness values identify sectors where destructive burial could occur even when conditional probabilities are moderate (0.2–0.6), representing low–frequency but high–severity outcomes critical for infrastructure design and emergency planning.

Topography and summit morphology strongly modulate sector exposure. Drainage confinement dominates routing in the lower–volume case. In the higher–volume simulations, the reduced modeled impact on the eastern flank reflects the central source configuration adopted for VolcFlow and the deflecting effect of the paleocrater, rather than an intrinsic reduction in hazard. The preserved eastern–flank PDC deposits show that this sector was inundated in the past, under vent or morphological configurations that differed from the present. A deterministic higher–volume scenario sourced from the northeastern flank (Section 6.3) confirms that a Fuego–scale event directed toward this sector would reach inhabited areas; notably, even under this forced configuration the present topography still redirects part of the flow toward the southern and northwestern flanks (Fig. S2), indicating that the eastern flank is not the natural travel path for PDCs under the current summit morphology. Eastern–sector communities should therefore not be considered intrinsically protected, and changes in eruptive style or vent location — such as column collapse or the development of a new eruptive center — could produce fundamentally different inundation patterns from those presented.

Hazard implications are sector–specific and scenario–dependent. The southern and southwestern sectors consistently show elevated potential impact due to the combination of high inundation probabilities and large maximum thickness values, affecting rural communities, agricultural estates, and key transportation corridors. Under higher–volume conditions, potential impact expands to major population centers (Santiago Atitlán) and additional road infrastructure. The eastern flank, although less affected in the probabilistic high–volume maps for the reasons noted above, remains exposed under the lower–volume ensemble and under the deterministic northeastern scenario.

This work complements existing multi–hazard zonation at Atitlán. Haapala et al. (2005) provided foundational zonation for lahars, tephra fall, and other volcanic processes. The probabilistic PDC hazard assessment presented here adds a quantitative component that can be integrated with lahar corridors and tephra–fall scenarios to support coherent multi–hazard planning, emergency management, and risk communication around Atitlán stratovolcano.

Acknowledgements

EPR visit to the University of South Florida was supported by SJC NSF CAREER award 1751905. This research was conducted with support from the project "Technical Cooperation for the SAT Project for Volcanic Eruption Preparedness in Guatemala and Central America", funded by the Swiss Agency for Development and Cooperation (COSUDE) and Asociación Vivamos Mejor Guatemala, with the support of Instituto Nacional de Sismología, Vulcanología, Meteorología e Hidrología (INSIVUMEH). Numerical computations benefited from the Research Computing resources and high-performance cluster facilities (CIRCE) at the University of South Florida (USF) and the computational resourses from the National Laboratory for Advanced Scientific Visualization (LAVIS) at Universidad Nacional Autónoma de México. The main author gratefully acknowledges the scholarship support provided by CONAHCYT (currently SECIHTI – Secretaría de Ciencia, Humanidades, Tecnología e Innovación).

Funding

This work was supported by the National Science Foundation, Faculty Early Career Development Program (CAREER) [Award No. 1751905] to S.J. Charbonnier; CONAHCYT (currently SECIHTI) through a doctoral scholarship to E. Pico Rodríguez; and the Swiss Agency for Development and Cooperation (COSUDE) and Asociación Vivamos Mejor Guatemala, through the project "Technical Cooperation for the SAT Project for Volcanic Eruption Preparedness in Guatemala and Central America," with support from the Instituto Nacional de Sismología, Vulcanología, Meteorología e Hidrología (INSIVUMEH).

CRediT authorship contribution statement

Eduard Pico Rodriguez: Field data collection, Data curation, Formal analysis, Investigation, Methodology, Visualization, Writing – original draft, Writing – review & editing.

Lucia Capra pedol: Conceptualization, Supervision, Data curation, Formal analysis, Funding acquisition, Investigation, Methodology, Project administration, Resources, Visualization, Writing – original draft, Writing – review & editing.

Sylvain Charbonnier: Methodology, Investigation, Resources, Supervision, Writing – review & editing.

Rafael Torres-Orozco: Investigation, Writing – review & editing.

Omar Cruz–Vázquez: Investigation.

Rudiger Escobar Wolf: Writing – review & editing.

672 **References**

673

674 AMSCLAE. (2018). *Priorización de Microcuencas*. www.amsclae.gob.gt

675 Andronico, D., Di Roberto, A., De Beni, E., Behncke, B., Bertagnini, A., Del Carlo, P., & Pompilio, M. (2018).
676 Pyroclastic density currents at Etna volcano, Italy: The 11 February 2014 case study. *Journal of*
677 *Volcanology and Geothermal Research*, *357*. https://doi.org/10.1016/j.jvolgeores.2018.04.012

678 Aravena, A., Tadini, A., Bevilacqua, A., Samaniego, P., Bernard, B., Hidalgo, S., Le Pennec, J.-L., Martínez-
679 Yáñez, P., García, J., & Roche, O. (2024). Probabilistic, scenario-based hazard assessment for pyroclastic
680 density currents at Tungurahua volcano, Ecuador. *Bulletin of Volcanology*, *86*(10), 84.
681 https://doi.org/10.1007/s00445-024-01768-y

682 ASF DAAC. (2014). *ALOS PALSAR High Resolution Radiometric Terrain Corrected Product*. NASA Alaska
683 Satellite Facility Distributed Active Archive Center. https://doi.org/10.5067/Z97HFCNKR6VA

684 Baxter, P. J. (1990). Medical effects of volcanic eruptions. *Bulletin of Volcanology*, *52*(7), 532–544.
685 https://doi.org/10.1007/BF00301534

686 Brown, S. K., Jenkins, S. F., Sparks, R. S. J., Odbert, H., & Auker, M. R. (2017). Volcanic fatalities database:
687 analysis of volcanic threat with distance and victim classification. *Journal of Applied Volcanology*, *6*(1),
688 15. https://doi.org/10.1186/s13617-017-0067-4

689 Capra, L., Rodríguez-Liñán, G. M., Torres-Orozco, R., Márquez-Ramírez, V. H., Sulpizio, R., & Arámbula, R.
690 (2024). Challenges in block-and-ash flow hazard assessment: The July 10–11, 2015 eruption of Volcán
691 de Colima, Mexico. *Journal of Volcanology and Geothermal Research*, *448*, 108050.
692 https://doi.org/10.1016/j.jvolgeores.2024.108050

693 Charbonnier, S. J., Garin, Franco., Rodríguez, L. A., Ayala, Karla., Cancel, Sahira., Escobar-Wolf, Rudiger.,
694 Chigna, Gustavo., Chun-Quinillo, Carla., González, Dulce., Chigna, William., Chun-Quinillo, Kevin.,
695 Mérida, Roberto., Juarez, Francisco., & Calder, E. S. (2023a). Unravelling the dynamics and hazards of
696 the June 3rd, 2018, pyroclastic density currents at Fuego volcano (Guatemala). *Journal of Volcanology*
697 *and Geothermal Research*, *436*, 107791. https://doi.org/10.1016/j.jvolgeores.2023.107791

698 Charbonnier, S. J., Germa, A., Connor, C. B., Gertisser, R., Preece, K., Komorowski, J.-C., Lavigne, F., Dixon,
699 T., & Connor, L. (2013). Evaluation of the impact of the 2010 pyroclastic density currents at Merapi

volcano from high-resolution satellite imagery, field investigations and numerical simulations. *Journal of Volcanology and Geothermal Research*, *261*, 295–315. https://doi.org/10.1016/j.jvolgeores.2012.12.021

Charbonnier, S. J., & Gertisser, R. (2009). Numerical simulations of block-and-ash flows using the Titan2D flow model: examples from the 2006 eruption of Merapi Volcano, Java, Indonesia. *Bulletin of Volcanology*, *71*(8), 953–959. https://doi.org/10.1007/s00445-009-0299-1

Charbonnier, S. J., Kelfoun, K., Widiwijayanti, C., Sayudi, D. S., & Putra, R. (2023b). *Assessing the Pyroclastic Density Current Hazards at Merapi: From Field Data to Numerical Simulations and Hazard Maps* (pp. 473–500). https://doi.org/10.1007/978-3-031-15040-1_16

Charbonnier, S. J., Thouret, J.-C., Gueugneau, V., & Constantinescu, R. (2020). New Insights Into the 2070calyrBP Pyroclastic Currents at El Misti Volcano (Peru) From Field Investigations, Satellite Imagery and Probabilistic Modeling. *Frontiers in Earth Science*, *8*. https://doi.org/10.3389/feart.2020.557788

Cisneros de León, A., Danišík, M., Schmitt, A. K., Schindlbeck-Belo, J. C., Kutterolf, S., Mittal, T., Garrison, J. M., & Sims, K. W. W. (2025). Refining the Eruption Chronology of Atitlán Caldera Through Zircon Double-Dating. *Geochemistry, Geophysics, Geosystems*, *26*(3). https://doi.org/10.1029/2024GC011953

Clarke, B., Tierz, P., Calder, E., & Yirgu, G. (2020). Probabilistic Volcanic Hazard Assessment for Pyroclastic Density Currents From Pumice Cone Eruptions at Aluto Volcano, Ethiopia. *Frontiers in Earth Science*, *8*. https://doi.org/10.3389/feart.2020.00348

de' Michieli Vitturi, M., Esposti Ongaro, T., Lari, G., & Aravena, A. (2019). IMEX_SfloW2D 1.0: a depth-averaged numerical flow model for pyroclastic avalanches. *Geoscientific Model Development*, *12*(1), 581–595. https://doi.org/10.5194/gmd-12-581-2019

Denlinger, R. P., & Iverson, R. M. (2001). Flow of variably fluidized granular masses across three-dimensional terrain: 2. Numerical predictions and experimental tests. *Journal of Geophysical Research: Solid Earth*, *106*(B1), 553–566. https://doi.org/10.1029/2000JB900330

Ewert, J. W., & Harpel, C. J. (2004). In harm's way: Population and volcanic risk. *Geotimes*, *49*(4), 14 – 17. https://www.scopus.com/inward/record.uri?eid=2-s2.0-2442626434&partnerID=40&md5=1427d30fc7650b796c56e3367acd0a12

Fischer, J.-T., Kowalski, J., & Pudasaini, S. P. (2012). Topographic curvature effects in applied avalanche modeling. *Cold Regions Science and Technology*, *74–75*, 21–30. https://doi.org/10.1016/j.coldregions.2012.01.005

Gueugneau, V., Charbonnier, S., Esposti Ongaro, T., de' Michieli Vitturi, M., Peruzzetto, M., Mangeney, A., Bouchut, F., Patra, A., & Kelfoun, K. (2021). Synthetic benchmarking of concentrated pyroclastic current models. *Bulletin of Volcanology*, *83*(11), 75. https://doi.org/10.1007/s00445-021-01491-y

Gueugneau, V., Kelfoun, K., & Druitt, T. (2019). Investigation of surge-derived pyroclastic flow formation by numerical modelling of the 25 June 1997 dome collapse at Soufrière Hills Volcano, Montserrat. *Bulletin of Volcanology*, *81*(4), 25. https://doi.org/10.1007/s00445-019-1284-y

Guimarães, L. F., Nieto-Torres, A., Bonadonna, C., & Frischknecht, C. (2021). A New Inclusive Volcanic Risk Ranking, Part 2: Application to Latin America. *Frontiers in Earth Science*, *9*. https://doi.org/10.3389/feart.2021.757742

Haapala, J. M., Wolf, R. E., Vallance, J. W., Rose, W. I., Griswold, J. P., Schilling, S. P., Ewert, J. W., & Mota, M. (2005). *Volcanic Hazards at Atitlán Volcano, Guatemala*.

Heim, A. (1932). *Bergsturz und Menschenleben / Albert Heim*. Fretz & Wasmuth A.G.

Helton, J. C., & Davis, F. J. (2003). Latin hypercube sampling and the propagation of uncertainty in analyses of complex systems. *Reliability Engineering & System Safety*, *81*(1), 23–69. https://doi.org/10.1016/S0951-8320(03)00058-9

INE. (2019). *XII Censo Nacional de Población y VII de Vivienda*.

Iverson, R. M., Schilling, S. P., & Vallance, J. W. (1998). Objective delineation of lahar-inundation hazard zones. *Geological Society of America Bulletin*, *110*(8), 972–984. https://doi.org/10.1130/0016-7606(1998)110<0972:ODOLIH>2.3.CO;2

Kelfoun, K. (2017). A two-layer depth-averaged model for both the dilute and the concentrated parts of pyroclastic currents. *Journal of Geophysical Research: Solid Earth*, *122*(6), 4293–4311. https://doi.org/10.1002/2017JB014013

Kelfoun, K., & Druitt, T. H. (2005). Numerical modeling of the emplacement of Socompa rock avalanche, Chile. *Journal of Geophysical Research: Solid Earth*, *110*(B12). https://doi.org/10.1029/2005JB003758

Kelfoun, K., Gueugneau, V., Komorowski, J., Aisyah, N., Cholik, N., & Merciecca, C. (2017). Simulation of block-and-ash flows and ash-cloud surges of the 2010 eruption of Merapi volcano with a two-layer model. *Journal of Geophysical Research: Solid Earth*, *122*(6), 4277–4292. https://doi.org/10.1002/2017JB013981

McKay, M. D., Beckman, R. J., & Conover, W. J. (1979). A Comparison of Three Methods for Selecting Values of Input Variables in the Analysis of Output from a Computer Code. *Technometrics*, *21*(2), 239. https://doi.org/10.2307/1268522

Montessus de Ballore, F. de. (1884). *Temblores y erupciones volcánicas en Centro-América*. Impr. del doctor F. Sagrini.

Newhall, C. G. (1987). Geology of the Lake Atitlán Region, Western Guatemala. *Journal of Volcanology and Geothermal Research*, *33*(1–3), 23–55. https://doi.org/10.1016/0377-0273(87)90053-9

Newhall, C. G., Paull, C. K., Bradbury, J. P., Higuera-Gundy, A., Poppe, L. J., Self, S., Bonar Sharpless, N., & Ziagos, J. (1987). Recent geologic history of lake Atitlán, a caldera lake in western Guatemala. *Journal of Volcanology and Geothermal Research*, *33*(1–3), 81–107. https://doi.org/10.1016/0377-0273(87)90055-2

Ogburn, S. E., & Calder, E. S. (2017). The Relative Effectiveness of Empirical and Physical Models for Simulating the Dense Undercurrent of Pyroclastic Flows under Different Emplacement Conditions. *Frontiers in Earth Science*, *5*. https://doi.org/10.3389/feart.2017.00083

Patel, P., Patra, A., & Charbonnier, S. (2022). Comment on Synthetic benchmarking of concentrated pyroclastic current models. *Bulletin of Volcanology*, *84*(6), 55. https://doi.org/10.1007/s00445-022-01561-9

Patra, A. K., Bauer, A. C., Nichita, C. C., Pitman, E. B., Sheridan, M. F., Bursik, M., Rupp, B., Webber, A., Stinton, A. J., Namikawa, L. M., & Renschler, C. S. (2005). Parallel adaptive numerical simulation of dry avalanches over natural terrain. *Journal of Volcanology and Geothermal Research*, *139*(1–2), 1–21. https://doi.org/10.1016/j.jvolgeores.2004.06.014

Patra, A. K., & Geophysical Mass Flow Group. (2023). *Titan2D: Geophysical Mass-Flow Simulation Software (Version 4.0.0) [User Guide]*.

Penfield, G. T., Rose, W. I., & Halsor, S. P. (1986). Geologic map of the Lake Atitlán volcanoes. *The Geological Society of America*.

Pico Rodriguez, E., Capra, L., Torres-Orozco, R., Secaira Ziegler, D. E., Chigna Marroquín, G. A., & Moncada Vásquez, M. (2026). Reassessment of the Holocene eruptive history of Atitlán stratovolcano, Guatemala. *Journal of South American Earth Sciences*, *173*, 105973. https://doi.org/10.1016/j.jsames.2026.105973

Pitman, E. B., Nichita, C. C., Patra, A., Bauer, A., Sheridan, M., & Bursik, M. (2003). Computing granular avalanches and landslides. *Physics of Fluids*, *15*(12), 3638–3646. https://doi.org/10.1063/1.1614253

Salm, B. (1993). Flow, flow transition and runout distances of flowing avalanches. *Annals of Glaciology*, *18*, 221–226. https://doi.org/10.3189/S0260305500011551

Salvatici, T., Morelli, S., Di Traglia, F., & Di Roberto, A. (2016). Runout modelling of gravity-induced pyroclastic density currents at Stromboli volcano (Italy). *Rendiconti Online Della Società Geologica Italiana*, *41*, 195–198. https://doi.org/10.3301/ROL.2016.127

Sapper, K. (1925). *Los volcanes de la América Central* (Vol. 1). Verlag Von Max Niemeyer.

Surono, Jousset, P., Pallister, J., Boichu, M., Buongiorno, M. F., Budisantoso, A., Costa, F., Andreastuti, S., Prata, F., Schneider, D., Clarisse, L., Humaida, H., Sumarti, S., Bignami, C., Griswold, J., Carn, S., Oppenheimer, C., & Lavigne, F. (2012). The 2010 explosive eruption of Java's Merapi volcano—A '100-year' event. *Journal of Volcanology and Geothermal Research*, *241–242*, 121–135. https://doi.org/10.1016/j.jvolgeores.2012.06.018

Torres-Orozco, R., Capra, L., Márquez-Ramírez, V. H., Sosa-Ceballos, G., De Plaen, R. S. M., Cid, H. E., Sulpizio, R., & Arámbula-Mendoza, R. (2024). Andesite magma genesis, conduit dynamics and variable decompression from shallow reservoirs drive contrasting PDC events at Volcán de Colima, Mexico. *Journal of Volcanology and Geothermal Research*, *453*, 108143. https://doi.org/10.1016/j.jvolgeores.2024.108143

Valentine, G. A. (1998). Damage to structures by pyroclastic flows and surges, inferred from nuclear weapons effects. *Journal of Volcanology and Geothermal Research*, *87*(1–4), 117–140. https://doi.org/10.1016/S0377-0273(98)00094-8

Voellmy, A. (1955). Über die Zerstörungskraft von Lawinen. *Schweizerische Bauzeitung*, *73*(12), 159–162.

Zuccarello, F., Andronico, D., Del Carlo, P., de' Michieli Vitturi, M., Di Roberto, A., Ganci, G., Behncke, B., Esposti Ongaro, T., Ciancitto, F., & Cappello, A. (2025). Trigger mechanism and propagation dynamics

of pyroclastic density currents at basaltic volcanoes. *Communications Earth and Environment*, *6*(1). https://doi.org/10.1038/s43247-025-02397-9

Tables

Table 1

Rheological parameters of Atitlán PDCs

Location	Type	Area (km^2)	Thickness (m)	Bulk Volume (Mm^3)	Friction coefficient
West flank	Fine-grained PDC	2.13	1.50	3.20	0.37
			0.80	1.71	0.36
			0.76	1.62	0.38
			0.34	0.72	0.38
			0.20	0.42	0.38
South flank	Fine-grained PDC	31.68	0.26	8.24	0.32
			2.00	63.36	0.28
North flank	Fine-grained PDC	2.37	1.50	3.56	0.42
			0.40	0.95	0.42
Northwest flank	BAF	3.15	8.00	25.18	0.37
			1.30	4.09	0.37

Note. Bulk volumes represent minimum and maximum estimates based on deposit thicknesses and inundation areas. Volumes are expressed in Mm^3 (10^6 m^3); the apparent friction coefficient (ΔH/L) is derived from the preserved deposit footprints only.

Table 2

Calibration parameters for *TITAN2D* and *VolcFlow*

Influx rate (m^3/s)	*Influx time (s)*	*Running time (s)*	*Volume (m^3)*
8	52	600	1.0×10^6
32	131	1200	1.0×10^7
170	301	1500	1.0×10^8

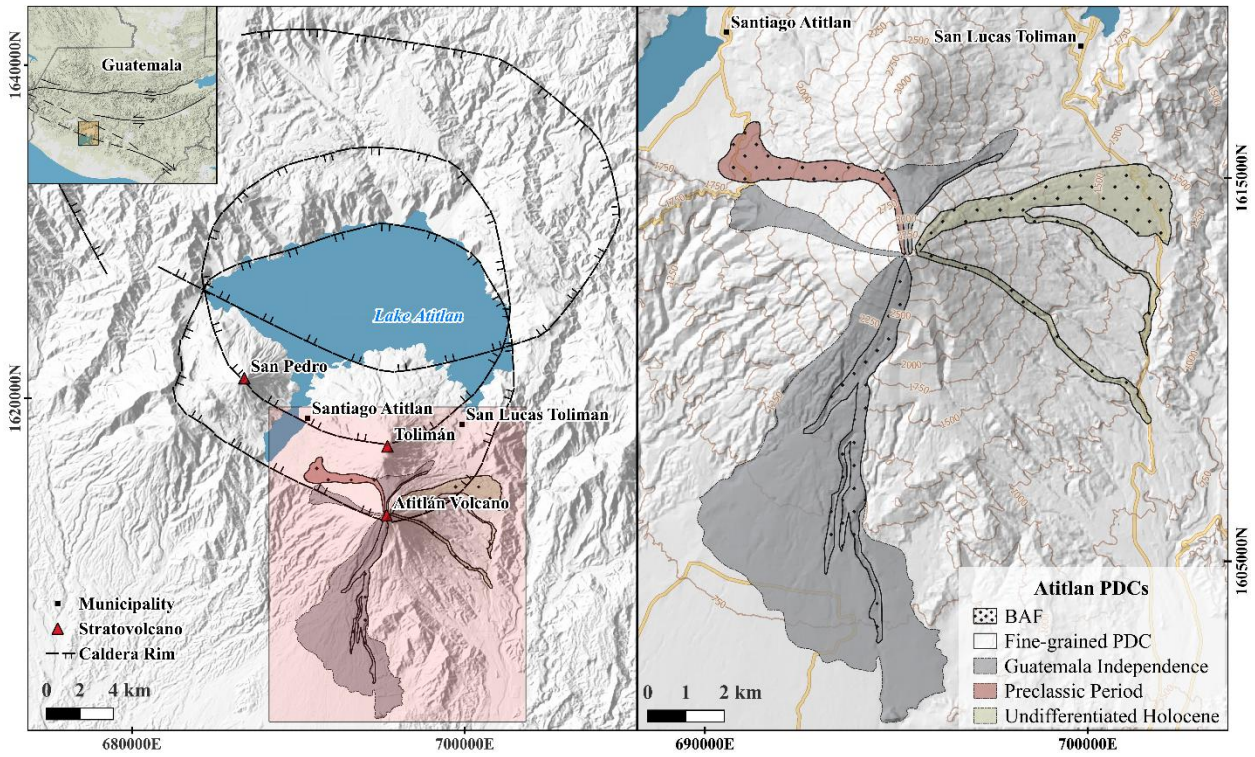
	TITAN2D		***VOLCFLOW***	
Source location	*X*	*Y*	*Row*	*Column*
	695180.0	1612848.7	1747	1079
Source radius	*meters*		*pixels*	
	55		4.4	
Rheology inputs	*Basal friction angle (μ)*		*Constant–Retarding stress (Pa)*	
	0.050		**2000**	
	0.075		2500	
	0.100		3000	
	0.125		3500	
	0.150		**4000**	
	0.175		4500	
	0.200		5000	

0.225	5500
0.250	**6000**
0.275	6500
0.300	7000
0.325	7500
0.350	**8000**
0.375	8500
0.400	9000
0.425	9500
0.450	**10000**
0.475	
0.500	

Note. Influx parameters selected to represent the variability of PDC deposits at Atitlán. The table lists the full set of rheological parameter ranges defined for model calibration, including basal friction coefficient (μ) values for *Titan2D* and constant retarding stress (CRS) values for *VolcFlow*. A representative subset of CRS values (bold) was simulated for each volume scenario, based on the systematic relationship between CRS and flow mobility (ΔH/L) identified during calibration (see Section 5.2 and Fig. 4).

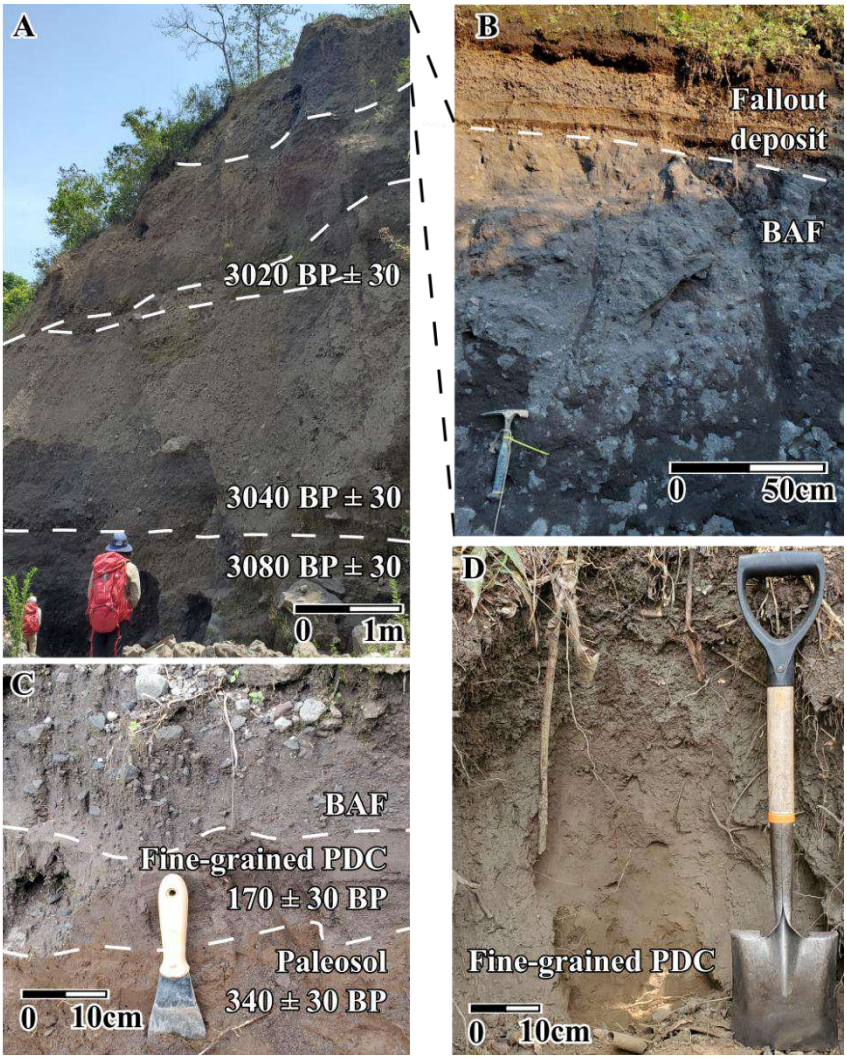
Figures

Figure 1



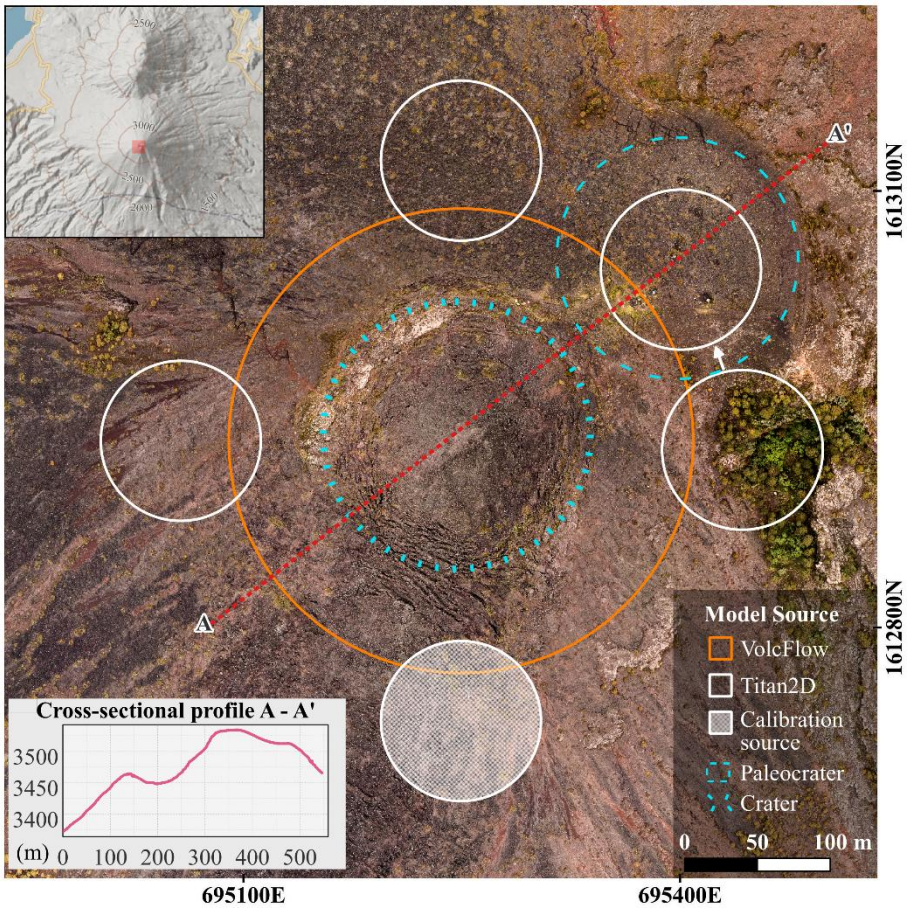
Localization and distribution of preserved PDC deposits at Atitlán stratovolcano and surrounding area. Mapped PDC deposits include BAF and fine–grained facies (Pico Rodriguez et al., 2026). Preclassic–period deposits are shown in red, undifferentiated Holocene deposits in green, and deposits associated with the last eruptive period (1826–1856) in gray. Major population centers – Santiago Atitlán and San Lucas Tolimán – are shown for reference. The mapped extents represent minimum preserved inundation areas and likely underestimate the original runout of past PDCs due to erosion and incomplete exposure.

Figure 2



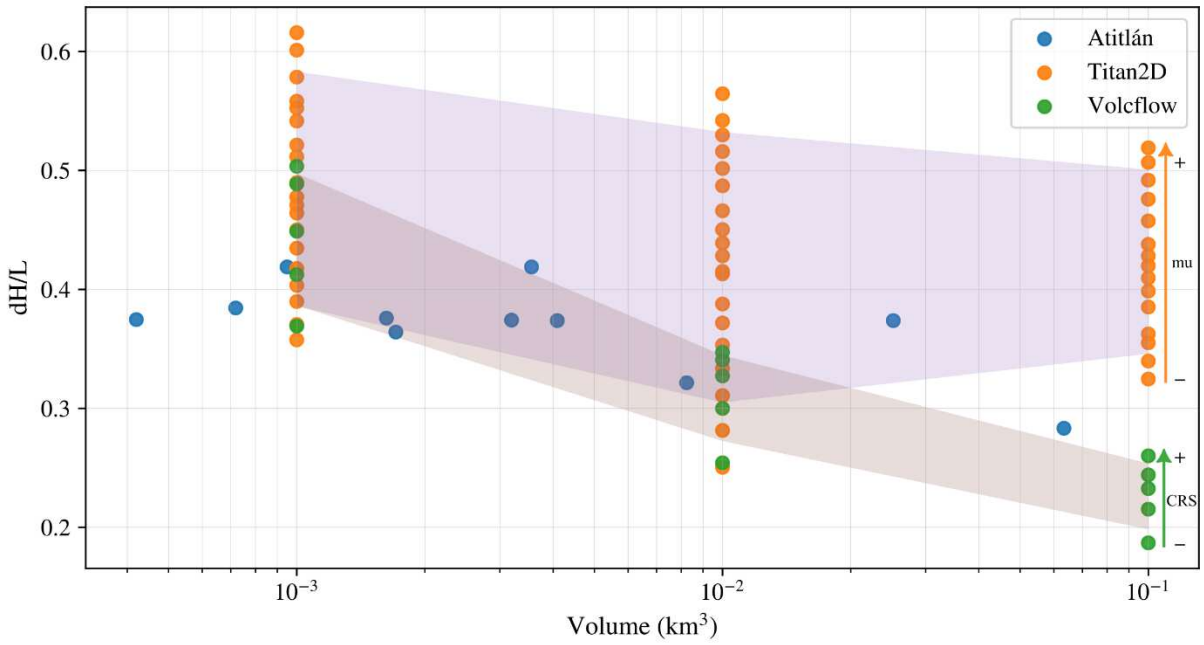
PDC deposits of Atitlán stratovolcano. (A) Massive BAF quarry from the Preclassic period (see Fig. 1), showing five distinct units. The outcrop is located northwest of the volcano along the road to Santiago Atitlán. (B) Upper contact of the massive BAF sequence with overlying fallout deposits. (C) Fine–grained PDC deposits from the most recent eruptive period (1826–1856 AD) covering the southern flank. (D) Fine–grained PDC deposits exposed on the northern flank related to the last eruptive episode. Figure modified from Pico Rodriguez et al. (2026).

Figure 3



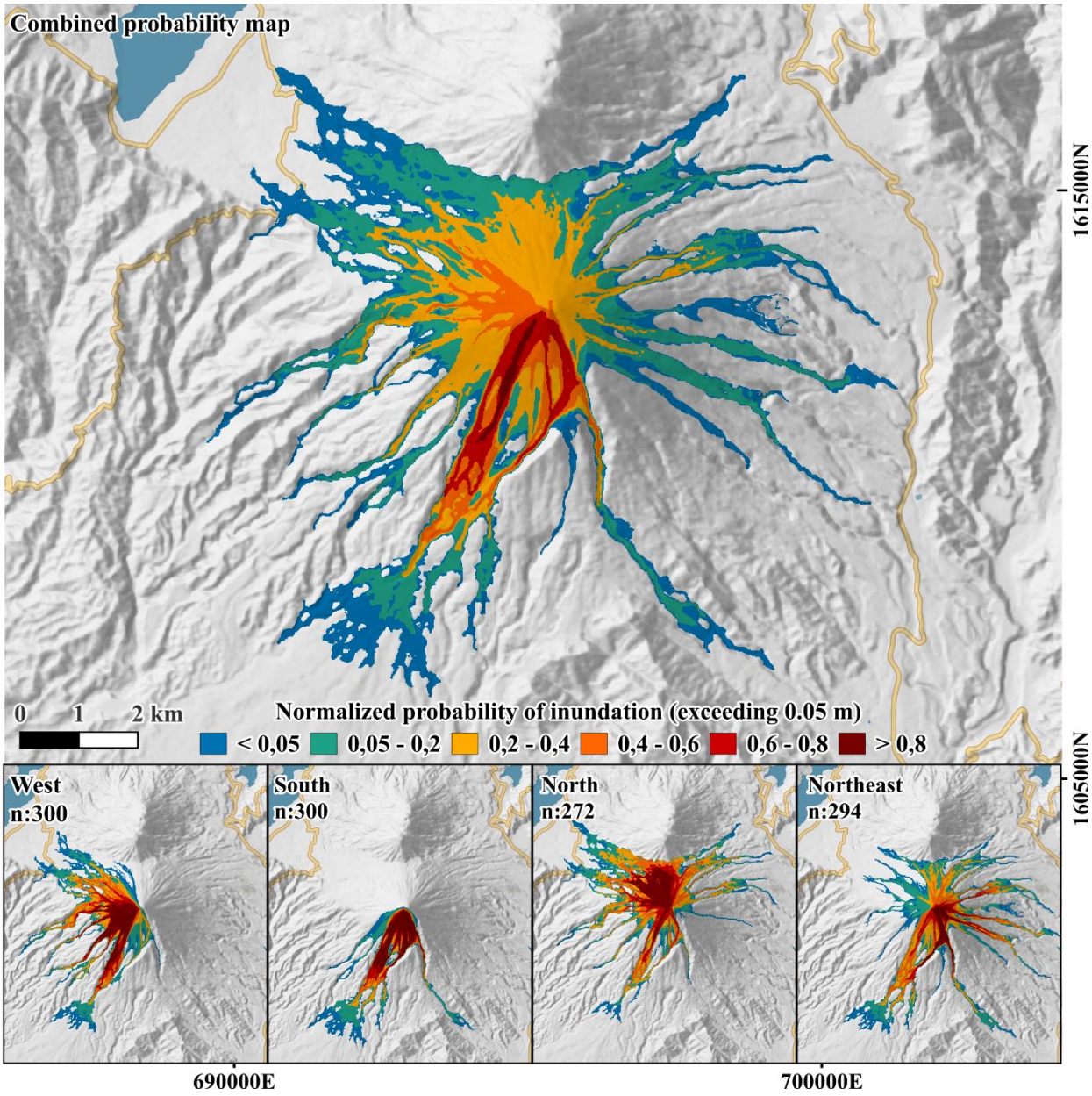
Source locations used in numerical simulations performed with *Titan2D* and *VolcFlow*. White circles (diameter 110 m), oriented toward the southern, western, northern, and northeastern flanks, represent PDC initiation sources used in *Titan2D* simulations. The northeastern source was positioned to account for topographic control (Cross–sectional profile **A–A'**) exerted by a paleocrater (cyan dashed line) that would otherwise divert eastward flows toward the south. For *VolcFlow* simulations, a single larger circular source (orange line; diameter 319 m) encompassing the summit area was used to represent high–volume scenarios.

Figure 4



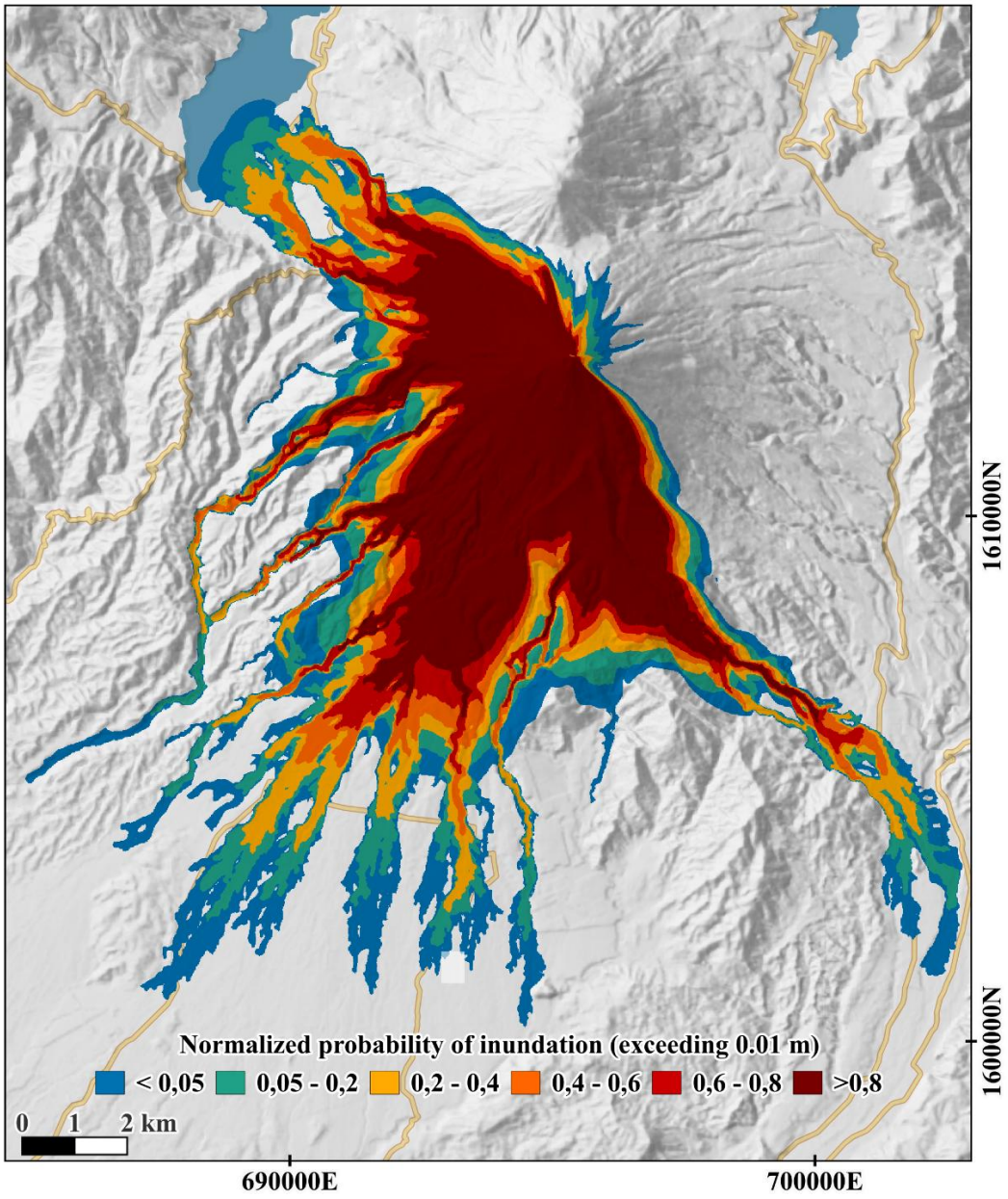
Model calibration: relationship between volume and mobility (ΔH/L) for PDC deposits at Atitlán (blue) and calibrated numerical simulations performed with *Titan2D* (orange) and *VolcFlow* (green). Model results correspond to simulations conducted under fixed source and volume conditions while sampling the selected ranges of basal friction coefficient (μ) and constant retarding stress (CRS). Shaded envelopes illustrate the interdecile range (P10–P90) of mobility values obtained for each model and volume scenario.

Figure 5



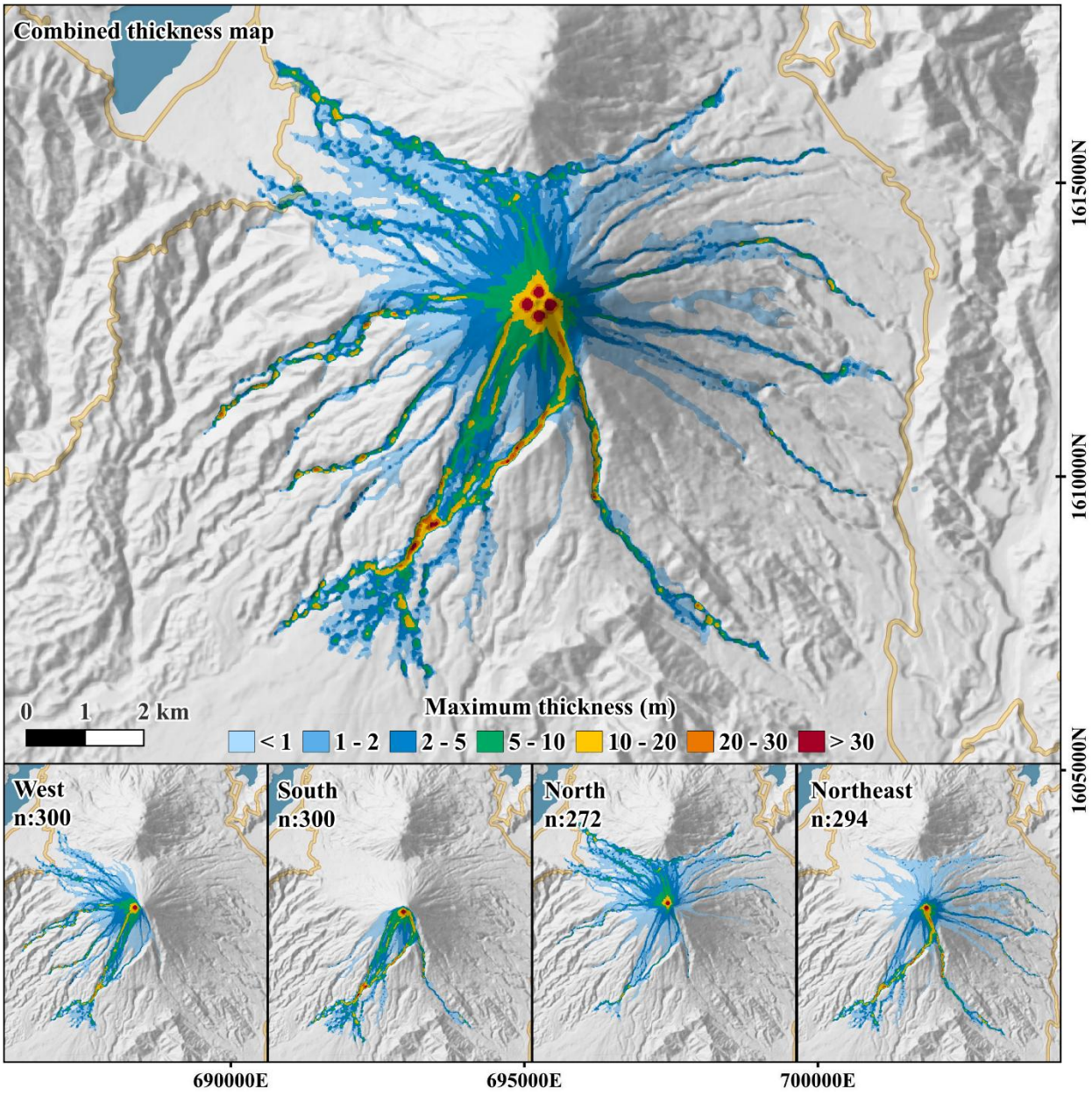
Probabilistic inundation patterns of the lower–volume PDC scenario (0.5–10 Mm³) simulated with *Titan2D*. The main panel shows the aggregated probability of inundation obtained by integrating the simulations from the four summit–oriented source locations (west, south, north, and northeast). Inundation probability represents the fraction of simulations in which flow thickness exceeds 0.05 m at each grid cell. Lower panels illustrate the individual probability maps for each source orientation and the number of iterations used for each source.

Figure 6



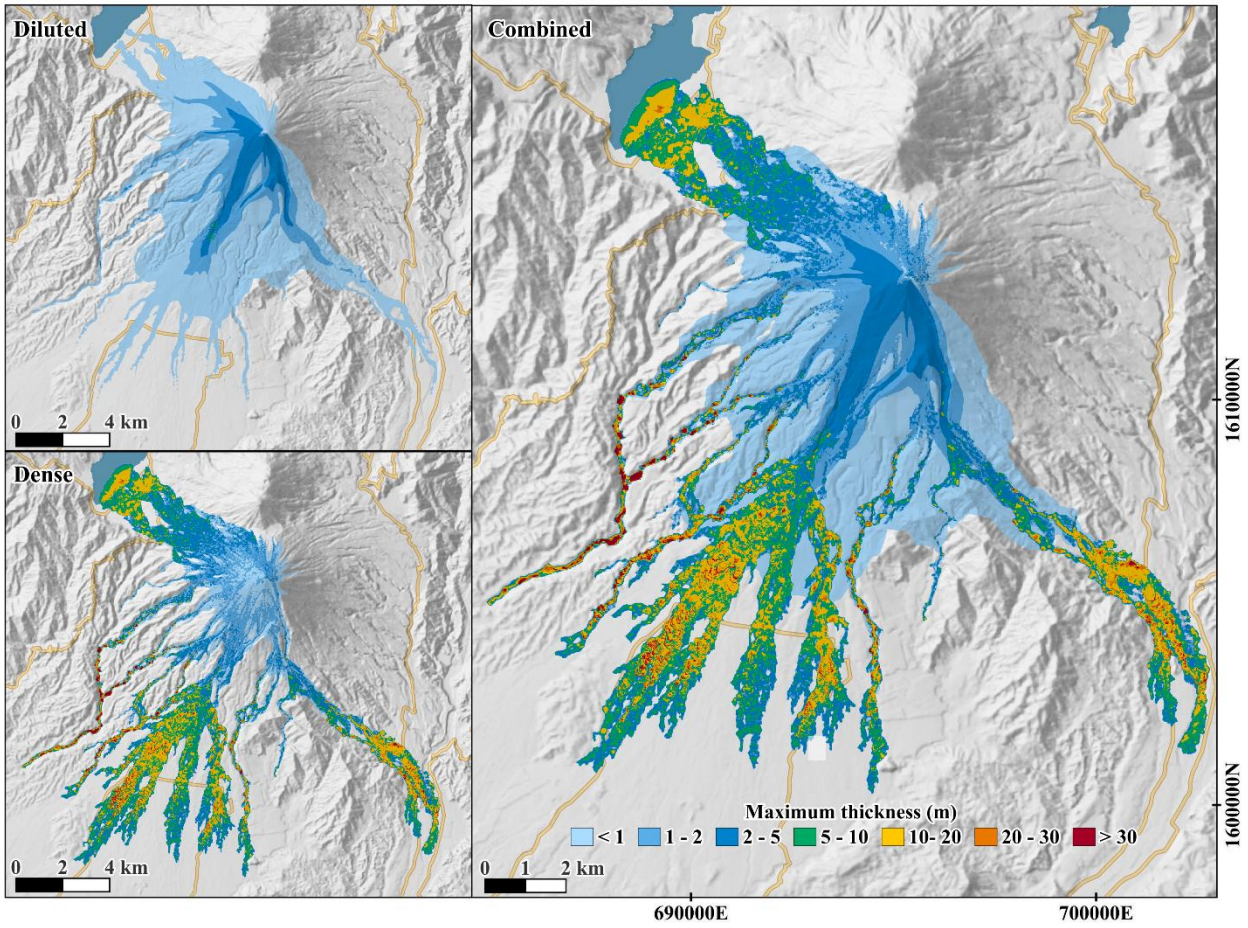
Probabilistic inundation patterns of the higher–volume PDC scenario (10–100 Mm^3) simulated with *VolcFlow*. Inundation probability (main panel) is defined as the fraction of simulations in which the PDC thickness exceeds 0.01 m at each grid cell.

Figure 7



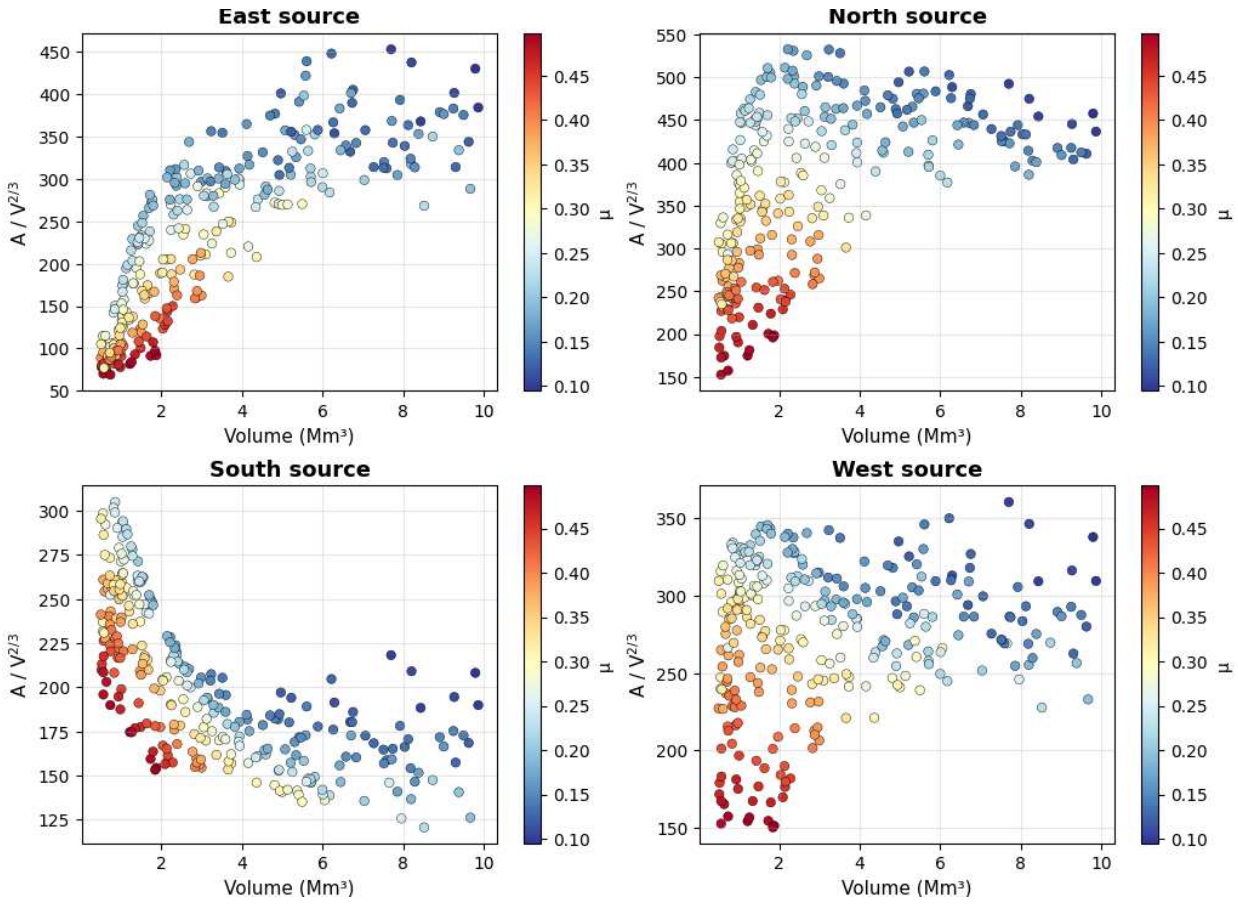
Maximum flow thickness map of the lower–volume PDC scenario (0.5–10 Mm³) simulated with *Titan2D*. Each color interval represents the maximum thickness value for each grid cell across all realizations.

Figure 8



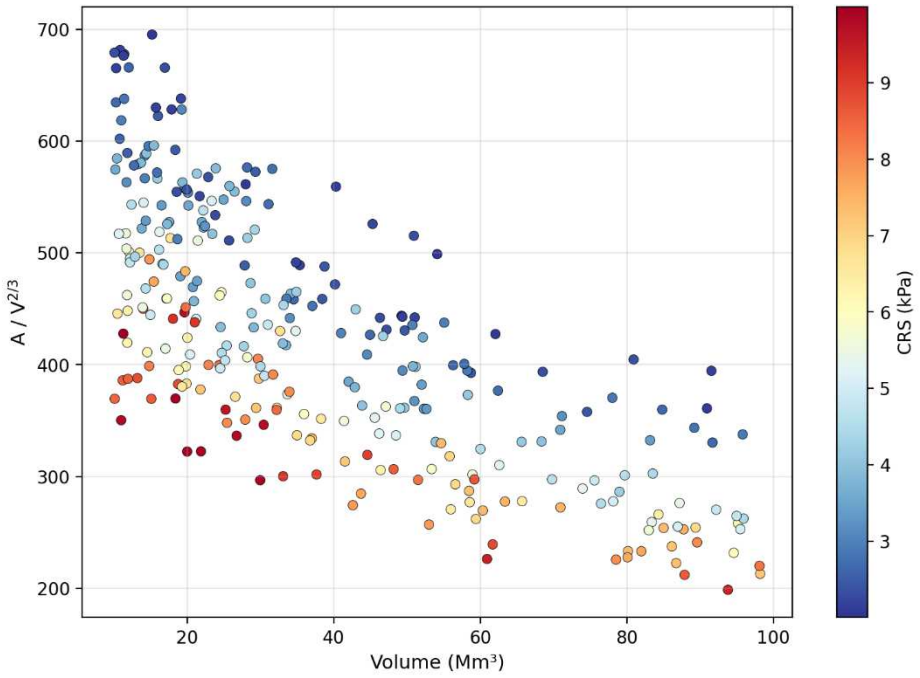
Maximum flow thickness map of the higher–volume PDC scenario (10–100 Mm^3) simulated with *VolcFlow*. Each color interval represents the maximum thickness value for each grid cell across all realizations. The main panel shows the aggregated thickness obtained by integrating the simulations from the dilute and concentrated phases produced by the model.

Figure 9



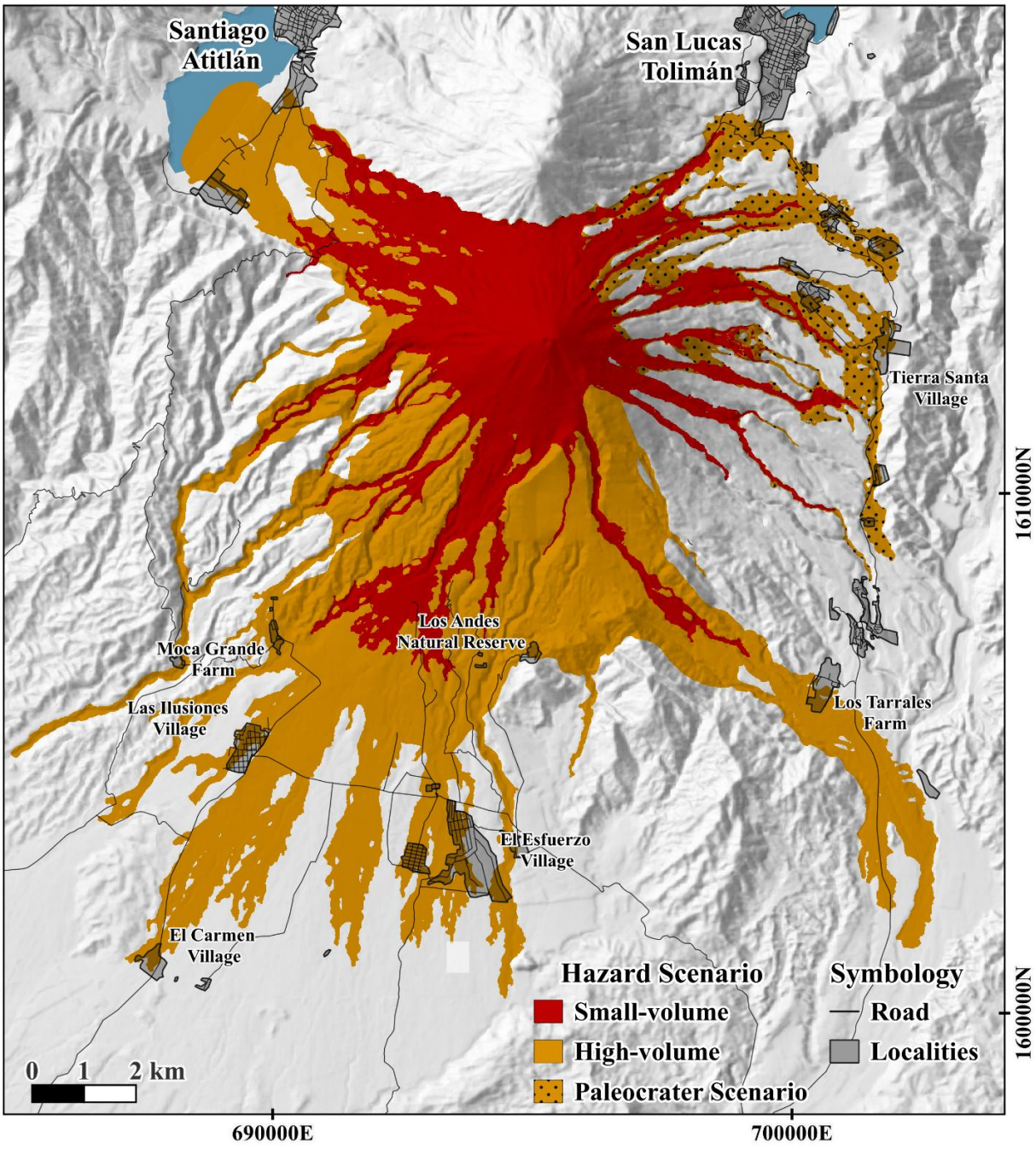
Mobility ratio ($A/V^{2/3}$) vs erupted volume for *Titan2D* simulations, grouped by source location. Each panel shows results for one of the four summit–oriented sources (East, North, South, West). Point color indicates the basal friction coefficient (μ). $A/V^{2/3}$ quantifies lateral spreading relative to flow volume — higher values indicate broader, less confined inundation footprints. The southern source shows a negative trend with volume, reflecting strong topographic confinement by deeply incised drainage channels, whereas the remaining sources show positive trends, indicating progressive overspill beyond channel margins as volume increases.

Figure 10



Mobility ratio ($A/V^{2/3}$) vs erupted volume for *VolcFlow* simulations. Point color indicates the constant retarding stress (CRS) value in kPa. $A/V^{2/3}$ decreases systematically with increasing volume, indicating that larger flows become proportionally thicker within existing channels rather than expanding laterally. Lower CRS values produce broader inundation footprints for equivalent volumes, consistent with reduced basal resistance in the concentrated flow. $A/V^{2/3}$ values for *VolcFlow* simulations exceed those of *Titan2D* (Fig. 9), reflecting the additional lateral spreading contributed by the dilute phase in the two–layer formulation.

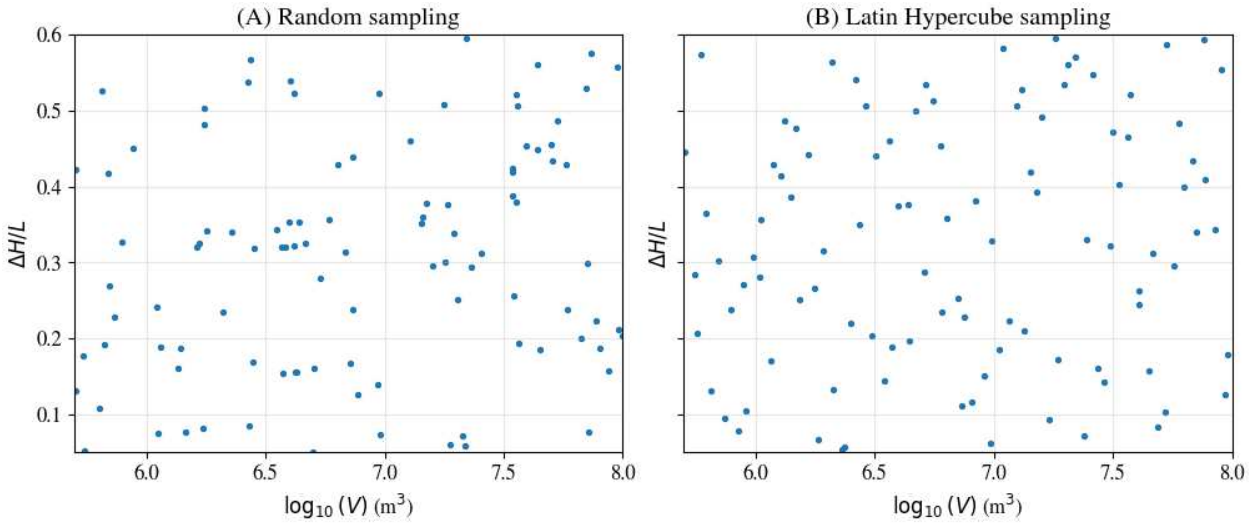
Figure 11



Binary inundation envelopes derived from *Titan2D* and *VolcFlow* simulations. Contours delineate areas where modeled thickness exceeded 0.05 m in at least one realization of each probabilistic scenario. The dotted polygon delineates the area where the deterministic northeastern–flank scenario (25 Mm^3; Supplementary Figure 13) exceeded 0.05 m. Settlements, infrastructure, and administrative boundaries are overlain to illustrate potential exposure. The map emphasizes maximum spatial reach.

Supplementary material

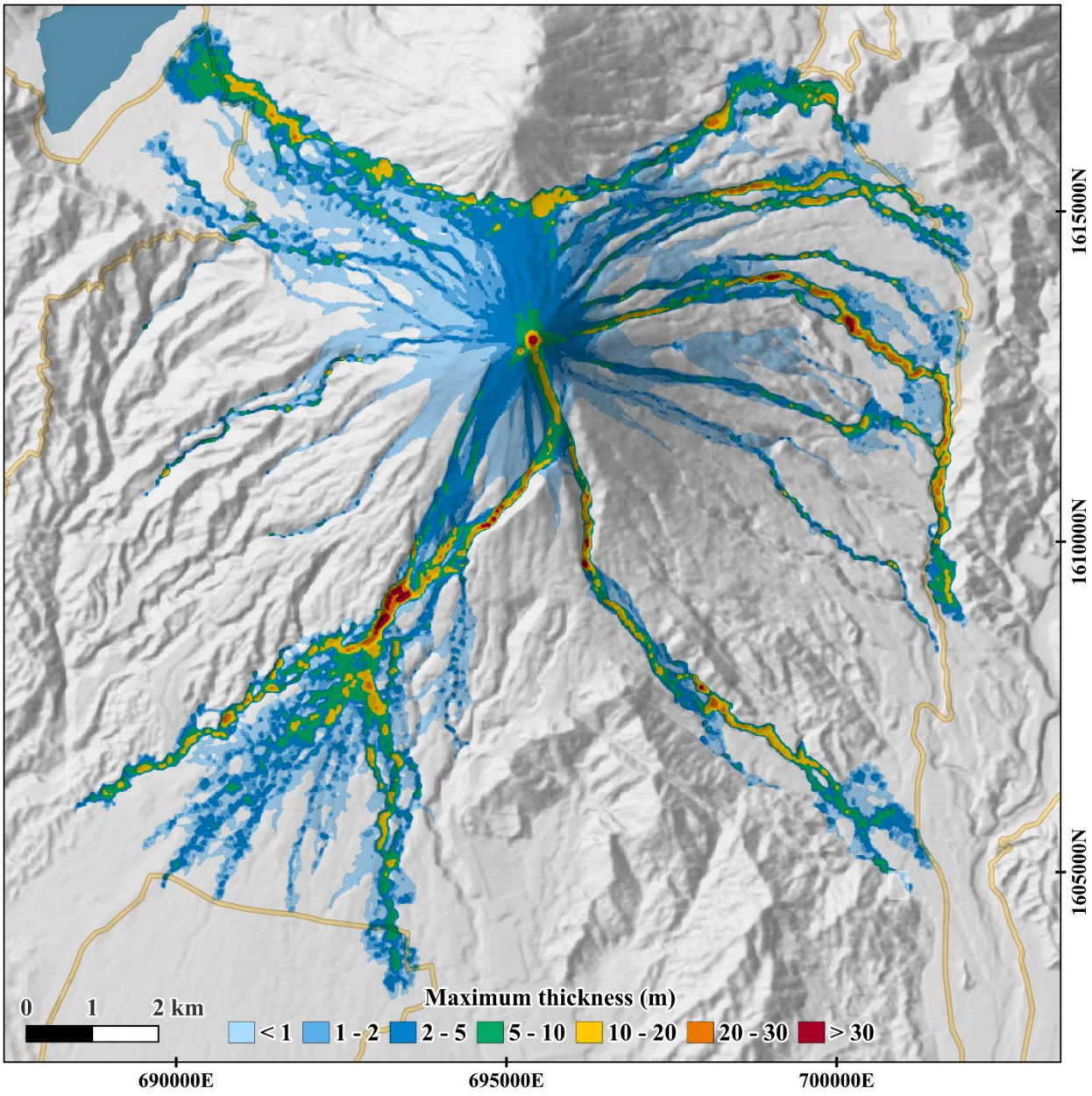
Figure S1



Conceptual comparison between random sampling (A) and Latin Hypercube sampling (B) applied to the same calibrated volume–mobility domain (100 points). Random sampling produces clustered distributions and poorly sampled regions, whereas Latin Hypercube sampling ensures a more uniform coverage of parameter space.

Latin Hypercube Sampling (LHS) is a stratified sampling technique that divides the range of each input parameter into equiprobable intervals and ensures that each interval is sampled exactly once. This method provides a more uniform and efficient coverage of multidimensional parameter space, reduces clustering of samples, and minimizes the number of simulations required to adequately explore parameter uncertainty (Fig. S1). This approach is particularly well suited for computationally demanding numerical models such as Titan2D and VolcFlow, where exhaustive sampling of all parameter combinations is impractical. By ensuring that the full range of calibrated volume–mobility conditions is sampled without redundancy, LHS allows robust probabilistic patterns to emerge with a limited ensemble size, while preserving the physical relationships between input parameters.

Figure S2



Maximum flow thickness map for the northeastern–flank deterministic scenario. A PDC of 25 Mm^3 was simulated with *Titan2D* from the NE source to evaluate the potential impact area of a higher–volume event comparable to the 2018 Fuego PDC (Charbonnier, Garin, et al., 2023). The map shows the envelope of maximum thickness across a range of basal friction coefficients (μ = 0.06–0.18). Unlike the probabilistic hazard maps, this single deterministic scenario is presented separately and is not incorporated into the probabilistic analysis.